DESIGN AND INVESTIGATION OF MOLECULAR NANOSTRUCTURES ON SURFACES WITH A LOW-TEMPERATURE SCANNING TUNNELING MICROSCOPE

by

Alexander Weber

B.Sc., University of Konstanz, 2001

M.Sc., Portland State University, 2003

A THESIS SUBMITTED IN PARTIAL FULFILMENT OF
THE REQUIREMENTS FOR THE DEGREE OF

MASTER OF SCIENCE

in

The Faculty of Graduate Studies

(Physics)

THE UNIVERSITY OF BRITISH COLUMBIA

14th April 2005

Abstract

Manipulating single surface atoms and adsorbates opens the possibility of structuring surfaces with atomic precision. This requires the use of a Low-Temperature Scanning Tunneling Microscope (LT-STM), which was assembled in this work. Atomic resolution data were obtained of closed packed metal surfaces at 18 K and standing wave patterns observed on Cu (111). Manipulation experiments with CO on Cu 111) were carried out to test the capabilities of the new instrument. In the course of this experiments the most recent imaging theory could be tested and the manipulation parameters of CO on Cu (111) optimized.

Contents

List of Figures

Acknowledgements

I want to express my gratefulness to the people who helped me to achieve this work.

Prof. Johannes Barth for being an excellent supervisor and taking really good care of his students.

My friends in the lab, namely Andreas Riemann, Wilhelm Auwärter and Agustin Schiffrin, for fruitful discussions, fun in the lab, teaching me about soccer and common evenings with a lot of good food.

Prof. George Savatzky for helpful discussions and CFI money for the project.

Prof. Tom Tiedje for being the second reader and showing me beautiful hikes around Vancouver.

My family for placing me in this world and making out of me what I am.

And last but definitely not least Karen Peters, for endless support and motivation.

Chapter 1

Introduction

The Scanning Tunneling Microscope (STM) is today one of the most powerful analyzing tools in nanoscale science. It allows a detailed image of a sample surface structure, down to atomic resolution. STM was invented by Binnig and Rohrer [1, 2] in the early 80's, enabling them to image the surface of Si (111)[3] with atomic resolution for the first time. For the design of the STM Binnig and Rohrer received the Nobel price in 1986 together with E. Ruska.

After the invention, this technique experienced a rapid development. One of the most important evolvements was the possibility to manipulate single molecules and atoms [4, 5, 6] by building Low-Temperature STMs. This opened a large bandwidth of applications: The artificial structuring of surfaces by positioning molecules and atoms with atomic precision [7], the assembly as well as the dissociation of single molecules [8, 9, 10] up to the artificial charging of atoms with single electrons [11].

For the structuring of surfaces it is necessary to freeze the mobility of surface atoms and adsorbates. Therefore Low-Temperature STMs (LT-STM) were developed which can operate at variable temperatures, from milli Kelvin range to room temperature. These LT-STMs allowed systematic studies of self-assembly phenomena, which is a promising field in nano science [12, 13, 14]. The ongoing miniaturizing of electronic structures pushes the

conventional semiconductor fabrication techniques to their physical limits. Therefore it is necessary to find novel ways to build miniature electronics through a bottom up principle. The investigation of self-assembled functional nanostructures goes in this direction.

In the group of Prof. Johannes Barth I got the possibility to assemble a Low Temperature STM.

The presented theses includes the assembly of a Low-Temperature STM, the calibration of the STM and carrying out first imaging and manipulation experiments.

CO molecules on Cu(111) were used for the manipulation experiments. The advantage of this system was that most of the parameter were known and could be used as a test of the new assembled LT STM. It was possible to optimize the manipulation parameters to decrease the time to assemble a nanostructure.

Furthermore it was possible to build small CO clusters and test the most recent imaging theories on this system. It was found that the appearance of single CO molecules could be described very well, but the image of clusters could not fully be explained on the base of this theories.

These experiments form the basic work with the new STM to begin our studies on self-assembled molecular nanostructures as well as performing spectroscopy experiments due to the stability of the new assembled LT-STM.

Chapter 2

STM basics

The Scanning Tunneling Microscope is experimentally a fairly simple setup and is simultaneously one of the most powerful tools in surface science. This chapter will be devoted to the STM theory. First the operation principles of STM will be demonstrated. In the second part the Tersoff Hamann approach will be presented, which was the first theoretical interpretation of the STM tunneling current and provides insight in its essential features.

2.1 Operation principles

STM exploits the quantum mechanical effect of electrons tunneling through a potential barrier. An atomically fine tip is brought 5 to 10 Å close to a surface, as shown in figure 2.1. The insulating vacuum between tip and sample forms a potential barrier, where electrons have a finite probability to tunnel through as schematically shown in figure 2.2.

By applying a bias voltage between tip and sample a measurable tunneling current (I_t) can flow. This current is exponentially dependent on the tip-sample distance and is very sensitive to distance changes:

$$I_t = I_0 e^{\frac{z}{z_0}} \tag{2.1}$$

The tunneling current is typically between 10^{-12} - 10^{-9} A. A change in the

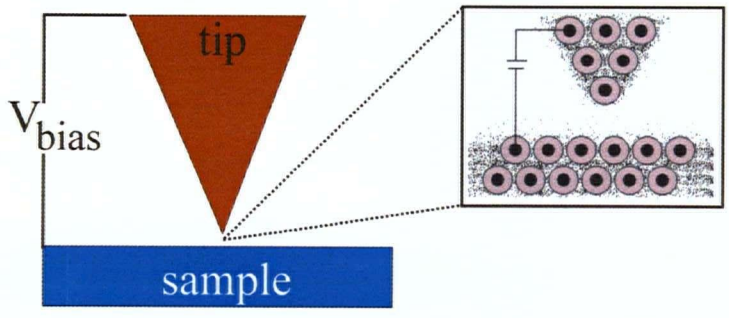

Figure 2.1: Schematic drawing of the tip and sample. The electrodes are typically 5-10 Å apart forming a vacuum barrier, where electrons can tunnel through. The magnified part shows a model of the atomic structure of tip and sample, where the dots represent the electronic clouds. The applied bias induces a tunneling current, which can be measured.

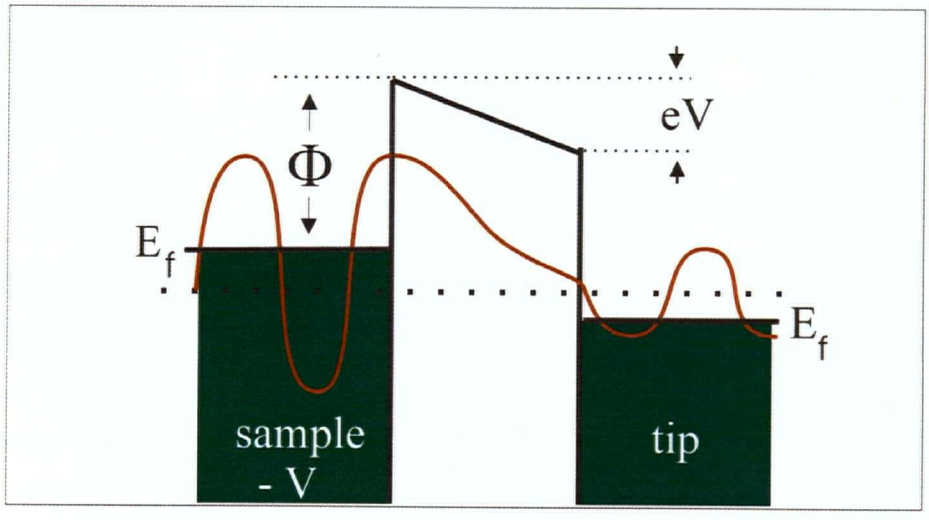

Figure 2.2: Schematic drawing of an electron wave tunneling from the sample through the vacuum potential barrier into the tip. The height of the potential barrier is the work function Φ. The applied bias is negative at the sample.

sample-tip distance of 1 Å changes the current about one order of magnitude. By measuring the tunneling current as a function of the tip position over the surface, topographic properties of the sample can be studied. Figure 2.3 gives an overview of the STM working principle. The tip is approached with a 3-dimensional piezo element to the sample until a tunneling current can be measured. This tunneling current is amplified and fed into the data acquisition board as well as into a feedback control. The feedback control regulates the tip height with the z-piezo whereas the x and y direction are controlled separately. In the constant current mode the tunneling current is set to a fixed value. The x and y control scan the tip row by row over the desired area and the feedback control keeps the current constant by moving the tip accordingly in z direction. The obtained image is the tip movement in z-direction over the the scan area.Another measuring mode is the constant height mode. The tip is kept at a fixed height above the sample during the scan. In this mode the changing tunneling current depending on the tips position is recorded. This mode is used less frequently, since it is more likely to crash the tip into the sample. However, its advantage is that it can be used to scan very fast over a well defined region.

A common parameter describing the tunneling conditions used for an image is the tunnel resistance $R_t = V_{bias}/I_t$. R_t ranges typically from 500 $M\Omega$ when the tip is still far away (10-15 Å) to 10M Ω where it is considered to be in contact with the sample. R_t is a useful indication for the applied parameters but not sufficient for reproducibility of an image. As will be explained later, the image contrast depends in many cases on the applied bias and the condition of the tip [15, 16]. Therefore it is more reasonable to

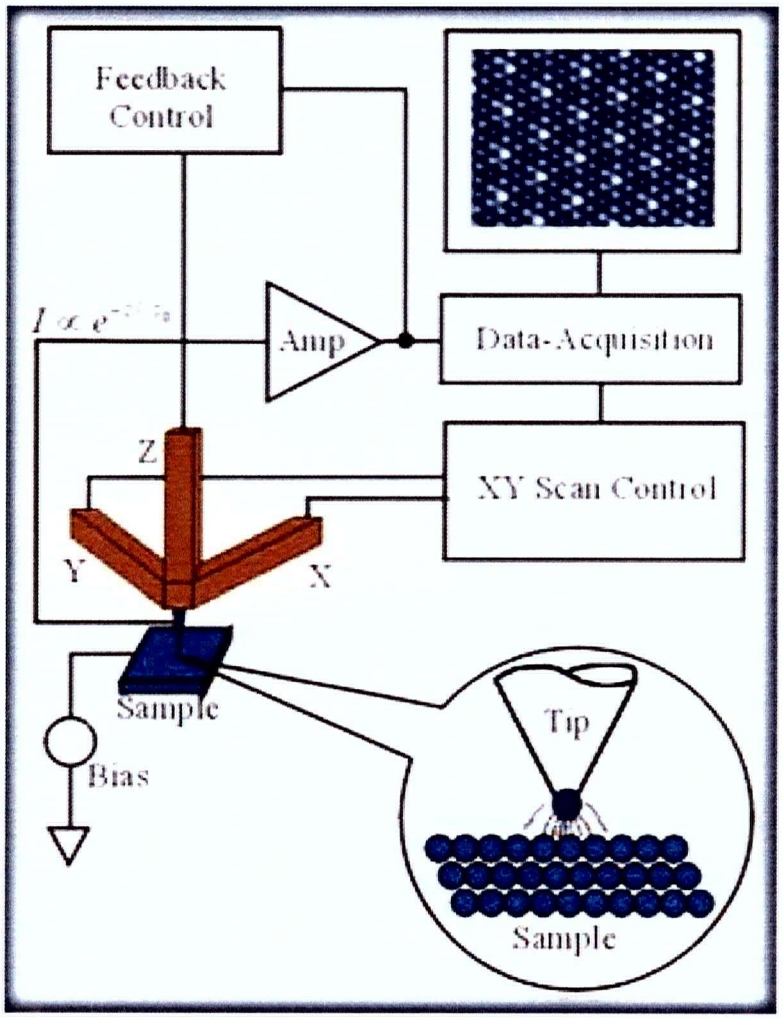

Figure 2.3: Schematic drawing of the STM working principle. The tip is approached to the sample and the piezo elements move the tip over the surface. The measured tunneling current is fed into a feedback control, regulating the height of the tip with the z piezo. The tunneling current or the z-movement, depending on the imaging mode, are used for the data acquisition, and the STM image is produced by the transformation of the tunneling current or z-piezo movement over the scanned area.

simply specify applied bias and tunneling current for the data.

The STM tip is the most important part of the STM and at the same time the most poorly defined. The goal is to get an atomically sharp tip, which means having at the apex of the tip one atom sticking further out towards the sample then the others. But for the contrast of the image the atomic structure of the apex is of importance too, as will be discussed in chapter 3. Furthermore the apex geometry can change during the scan, which makes the tip well defined only for the initial scans [17]. There are different attempts to model the tip [16] but they are limited due to the described problems making a realistic model almost impossible. However, there are some simplified tip models which allow the qualitative interpretation of the obtained images, as will be discussed below.

The tip conditions are not the only factors limiting the resolution of the STM image. Important issues are also interfering mechanical ,electrical vibrations, the type of piezo elements used and a high STM eigenfrequency.

Mechanical vibrations can be caused by the building (10 to 20 Hz), and higher frequent waves caused by acoustic signals. Therefore the whole instrument usually is vibrationally damped by sitting on pneumatic vibration isolators, hanging on springs from the ceiling or active vibration controls. Furthermore, eddy current brakes in the STM itself are used to decouple the STM from interfering vibrations.

Electrical noise is reduced by using preferably an independent ground as well as the use of BNC cables. For some occasions it is necessary to use low pass filters.

The type of piezos used has an influence on interfering vibrational noise

as well. Tube piezo elements are the most commonly used, since they have a high Eigen-frequency and are therefore less likely to be excited. An additional advantage to single stage piezos is that the different directions in a tube piezo interfere each other less resulting in more stable imaging conditions. The tube piezos used have typically a distance change of 10 Å/V at room temperature, resulting in a resolution of down to 1 pm.

2.2 STM theory

There are several theories to describe the tunneling current I_t [16, 18]. The first theory has been developed by Tersoff and Hamann [19, 20]. Since it is a physically descriptive model and is still used to interpret experimental results their approach will be described in the following section.

Tersoff and Hamann used the transfer Hamilitonian approach to calculate the tunneling of electrons from one electrode to another, separated by vacuum as shown in figure 2.2. An electron wave in the sample approaches the vacuum barrier. The potential barrier has the height Φ, representing the work function of the sample and the tip. Part of the wave tunnels through the potential barrier decreasing its amplitude exponentially, representing the decreasing tunneling probability. Once the electron has tunneled through the barrier it arrives in the tip and can be measured as a tunneling current if a bias is applied. An applied bias voltage of x V changes the fermi level of the tip compared to the sample by x eV. By changing the polarization of the bias, the tunneling direction is reversed.

In first order perturbation theory the tunneling current between two sep-

arated electrodes is calculated as follows:

$$I_t = \frac{2\pi e}{\hbar} \sum_{\mu,\nu} [f(E_\nu) - f(E_\mu)] |M_{\mu,\nu}|^2 \delta(E_\nu + eV - E_\mu) \tag{2.2}$$

Here $f(E)$ is the Fermi function, V the applied bias voltage, $M_{\nu,\mu}$ the tunneling matrix element between the states Ψ_μ and $\Psi\nu$, of the left and right electrode. E_μ and E_ν are the energy levels of the states relative to the Fermi level in the left and right electrode.

At this point certain approximations have to be made to continue the calculation.

The first is to replace the Fermi function with a step function, which is in most of the cases valid due to low temperatures. The second approximation is to assume the applied bias to be small compared to the work function and therewith the expression simplifies to

$$I_t = \frac{2\pi e^2 V}{\hbar} \sum_{\mu,\nu} |M_{\mu,\nu}|^2 \delta(E_\mu - E_F) \delta(E_\nu - E_F) \tag{2.3}$$

To calculate $M_{\mu,\nu}$, Tersoff and Hamann used the matrix element calculated by Bardeen [20]:

$$M_{\mu,\nu} = \frac{\hbar^2}{2m} \int dS \cdot (\Psi_\mu^* \nabla \Psi_\nu - \Psi_\nu \nabla \Psi_\mu^*) \tag{2.4}$$

This integral is taken over any surface, which lies entirely in the barrier region and separates the two half spheres. To use this matrix element a further assumption has to be made, namely that the two wave functions are independent of each other, representing solutions from isolated electrodes.

In the next step Tersoff and Hamann used the following ansatz for the

electron wave function of the sample:

$$\Psi_\nu = \Omega_s^{-\frac{1}{2}} \sum_G a_G \cdot exp(-\sqrt{\kappa^2 + |\vec{k}_\parallel + \vec{G}|^2 r_\perp}) \cdot (i(\vec{k}_\parallel + \vec{G}) \cdot r_\parallel). \quad (2.5)$$

Here $\kappa = \frac{\sqrt{2m\phi}}{\hbar}$ is the minimum inverse decay length for the wave function in vacuum, ϕ the work function, Ω_s the sample volume, $\vec{G}$ the surface reciprocal-lattice vector and $\vec{k}_\parallel$ the surface Bloch wave vector.

For the tip they assumed the wave function to be spherically symmetric and therefore s-type like as shown in figure 2.4. R is the local radius of curvature, r_0 the location of the center of curvature and d the distance of the tip to the surface. Therewith the assumed wave function becomes:

$$\Psi_\mu = \Omega_t^{-\frac{1}{2}} c_t \frac{\kappa R e^{\kappa R}}{\kappa |\vec{r} - \vec{r_0}|} \cdot exp(-\kappa |\vec{r} - \vec{r_0}|), \quad (2.6)$$

where Ω_t is the probe volume, c_t a normalization factor, κ is defined as above and the work function of the tip is assumed to be the same as that of the sample.

Using these wave functions the following matrix element is obtained:

$$M_{\mu,\nu} = \frac{2\Pi\hbar^2}{m} \Omega_t^{-\frac{1}{2}} R e^{\kappa R} \sum_\nu |\phi(\vec{r_0})|^2 \delta(E_\nu - E_F). \quad (2.7)$$

Inserting this result into the initial formula for the tunneling current leads to the current:

$$I = \frac{32\Pi^3 e^2 V \phi^2 R^2 e^{2\kappa R}}{\hbar \kappa^4} D_t(E_F) \cdot \sum_\nu |\Psi_\nu(\vec{r_0})|^2 \delta(E_\nu - E_F), \quad (2.8)$$

where $D_t(E_F)$ is the density of states per tip unit volume.

The local density of states (LDOS) at the Fermi energy and the location

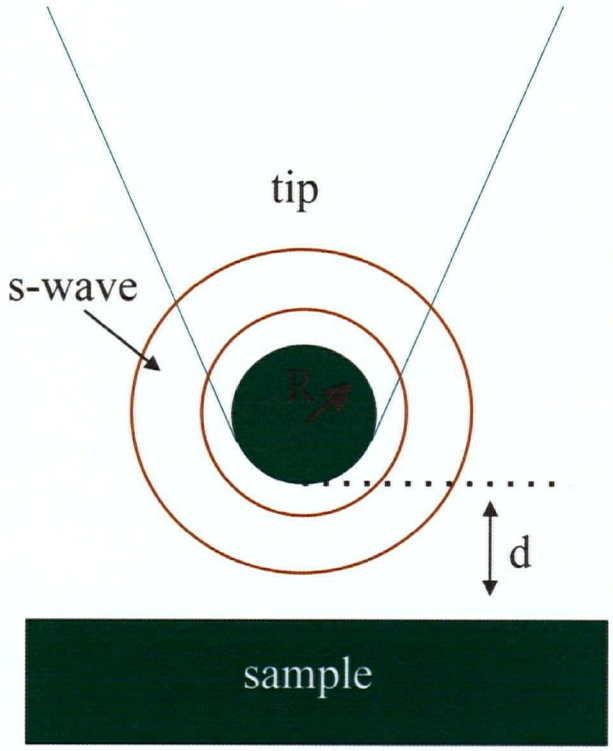

Figure 2.4: Schematic drawing of the assumed s-wave of the electron states of the tip in the Tersoff Hamann model.

of the tip is

$$\rho(\vec{r_0}, E_F) = \sum_{\nu} |\Psi_\nu(\vec{r_0})|^2 \delta(E_\nu - E_F). \tag{2.9}$$

That means that the current is proportional to the LDOS at the Fermi level and the location of the tip:

$$I \propto \rho(\vec{r_0}, E_F). \tag{2.10}$$

This model gives a principle understanding of the experimentally observed corrugation. The topography seen in STM images reflects the density of states which must not necessarily coincide with the geometry of a molecular or solid lattice. More advanced theories revealing more details come to the same conclusion, namely that the current is proportional to the density of states but are often less descriptive. Therefore the Tersoff-Hamann-model is still used to interpret experimental results.

However, there are some problems with this model [21]:

First, the assumption of a small bias compared to the work function can not be justified for imaging e.g. semiconductors where higher biases have to be used.

Second, the wave functions of tip and surface are assumed to be independent and therewith having no overlap. This is in particular not valid for high resolution images, where the distance between tip and sample is very close and therefore the wave functions influence each other which leads to a change of the electronic structure of the surface. Therefore strictly speaking it is not a perturbative ansatz, which Fermi's golden rule starts from.

Third, the surface wave function does not include electron interactions of the surface electrons.

Fourth, the assumption of the s-wave like tip function is a severe limitation.

There are further developments of the Tersoff-Hamann-model (THM) by Chen [22] where the tip function is assumed to be d-wave like and the model is able to explain atomic resolution on metals.

For further reading the following literature can be useful: The article of Werner A. Hofer [16] gives an outline of the present models, and a deeper discussion of the basics of these models is presented in "Scanning Tunneling Microscopy 3" [23].

Chapter 3

Imaging of adsorbates

A fascinating STM application is the imaging and manipulation of adsorbates. Their contrast in the image is vital information about the interaction with the surface, which plays a key role for the further development of nanostructures by controlling the adsorption sites with atomic precision. Therefore, this chapter will be devoted to the imaging of adsorbates on metallic surfaces. In the general part I will discuss how the tip shape, the tip-to-sample distance, and the applied bias influence the contrast of adsorbates. Then in part 3.1 I will give a general overview along Lang's pioneering work [24, 25] of modeling the contrast of adsorbates and I will demonstrate the validity of this model for imaging single adatoms. Moreover, I will briefly discuss the limitation of Lang's model. In the last part 3.2, I will give an introduction of modeling complex systems on metallic surfaces along Sautet's work [26] and give a short overview of the Green's function approach [27, 28].

To begin the general discussion of imaging it must be mentioned, that the contrast does not depend alone on the adsorbate-substrate interaction, but also on the condition of the tip, the tip-sample distance and most importantly the applied bias itself. These three parameters will be discussed briefly below.

A fairly intuitive argument for the influence of the tip shape is that a flat tip resolves maximally the atomic steps of surface terraces, whereas a sharp tip resolves the corrugation of the atomic lattice of the substrate. However,

the difference goes beyond this simple distinction. As already mentioned, the tip wave function is often modeled as an s-wave. Chen [29, 30] showed that the THM explains satisfyingly atomic corrugation only if the tip state is assumed to be a p or d-wave. This can yield to a modified appearance of adsorbates compared to the s-band calculation, which retroactive changes the interpretation of the image.

Furthermore, the atomic structure of the tip apex itself influences its electronic structure and therewith the image contrast. Tsukada at al. [31] showed that depending on the crystal geometry of a tungsten (W) tip, the contrast of graphite changes due to differently localized tip wave functions. That means that the observed corrugations can change their orientation to each other depending on the tip state contributing to the tunneling current. This effect can be especially critical for spectroscopy.

The tip-sample distance is another important factor. This is obvious for extreme cases, where the tip can drag the adsorbate along while being too close to the surface, or when being too far away loosing tunnel contact. Furthermore, depending on the distance, it is possible that different surface states have a different weight in the tunneling current. If the tip is very close to the surface it can furthermore influence the wave functions of the surface states and distort them.

Changing the bias voltage can affect the appearance of adsorbates as well. Depending on the applied bias, different electronic states contribute to the tunneling current, which can display different structures of the adsorbate in the image. Solving the transfer Hamiltonian like in the THM, a low bias voltage is assumed.

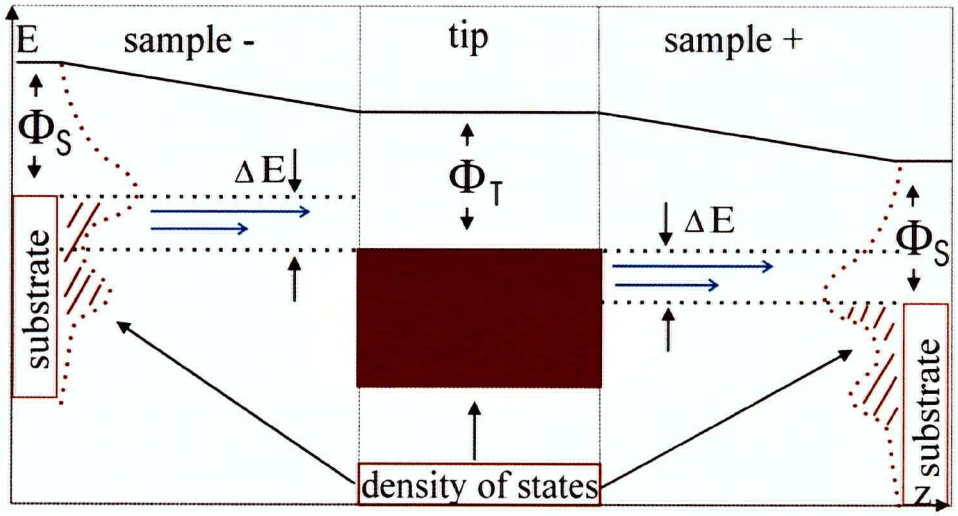

Figure 3.1: Schematic energy diagram for the tunnel contact between an adsorbate covered metal surface and the tip. The adsorbates density of states is shown as the red dotted lines, sitting on the substrate. The left junction represents the tunneling conditions for a negative applied bias. The right junction represents the situation for a positive applied bias [32].

For a finite applied bias voltage V, the range of electronic states $|Ef, Ef + eV|$ is contributing to the total tunneling current by integrating over this energy range. Hence, electronic states with energies different from the Fermi level can still contribute to the tunneling current via tails of resonance at the Fermi level, if their energies lie in the probed range (orbital mixing)[26].

Adsorbates can therefore show up as protrusion, depression or being even invisible for certain bias windows. Furthermore, they can appear in different geometrical forms depending on the electronic states involved in the tunneling current.

3.1 Adatoms

As discussed in the previous chapter, the STM maps the density of states of the surface and not its real geometrical structure, which coincides only for metallic adatoms on a metal surface. This differentiation is especially important for imaging some molecules, e.g. CO on Cu(111) [33], where the CO molecules which sit on top of the Cu lattice sites appear as depressions. To explain such phenomena different models were developed. It has to be noted that the imaging mechanism especially of complex molecules is still not fully understood.

However, Lang's [24] approach to interpret the contrast in STM images used the jellium model, where the ionic lattice of each metal is smeared out into a uniform positive charge background. The tunneling current is calculated again using Bardeens transfer Hamiltonian [20].

This model describes how a single adatom modifies the local density of states (LDOS) at the Fermi energy compared to the bare metal surface. Depending on the modification of the LDOS, the adsorbate is shown in the image as a protrusion or depression.

Figure 3.1 shows a schematic energy diagram for the tunnel contact between a metallic tip and a metallic surface with additional adsorbates. The vertical axis represents the energy and the horizontal axis the distance. The left and the right side show the density of states (red) of the sample, on the left with a negative sample bias and on the right with a positive bias. The tip's density of states (center, red) is assumed to be constant in the jellium model as well as in the Tersoff Hamann Model. Φ_s and Φ_t are the work function of the sample and the tip, respectively. In the left junction electrons

tunnel from the occupied states (hatched red) of the sample into unoccupied states of the tip, whereas in the right junction electrons from the occupied states of the tip tunnel into unoccupied states of the sample. The states of highest energy carry most of the current since they "see" a smaller energy barrier (indicated by the longer blue arrows).

An additionally important factor for the tunneling current is the form of the participating wave function: s-states are more delocalized than for example d-states and can therefore contribute more to the tunneling current as long as they contribute to the DOS at the Fermi level. The same argument applies to the p states. The p_z states are localized but oriented perpendicular to the surface towards the tip and therefore contribute to the tunneling current. The in-the-plane localized p_x and p_y states contribute very little. This is an important symmetry argument which is used for different imaging models.

To illustrate this model, Lang's results on a single sodium (Na) atom on a metallic surface [25] will be discussed briefly. Figure 3.2 shows schematically the atomic density of the Na 3s states with respect to the Fermi level of a bare metal surface. These states are energetically higher but still have an overlap with the Fermi level and the DOS increases. Therefore, the LDOS at the Fermi level at the position of the tip increases as well, which explains that a Na atom on a surface is imaged as a protrusion. Helium (He) on the other hand appears as a depression. Its closed shell does not contribute to the DOS, however, due to its different electronegativity it polarizes the electrons in the surface and changes therewith the DOS.

Another prominent example is Xe on Cu (111) [34] which has an energy

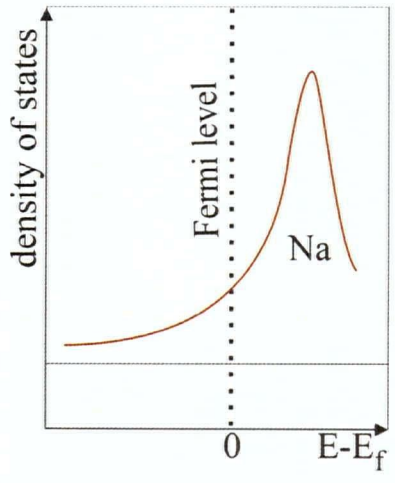

Figure 3.2: Schematic diagram of the density of states versus the energy of a Na adsorbate compared to the fermi level of a metal substrate[25]. The unoccupied 3s state tail resonates with the fermi level and therefore contributes to the DOS.

gap of 10 eV. The lowest unoccupied state, the Xe's 6s state, overlaps to a small amount with the Fermi level and extends further into the vacuum then the 3d states of Cu and therefore increases the LDOS at the position of the tip. Therefore it appears as a protrusion in STM. This example shows furthermore that insulators can be imaged with an STM under certain conditions [35, 36].

The interpretation of images with adsorbates like e.g. Oxygen (O) on Ni (100) [37], which chemisorbs on metal surfaces and therefore changes the electronic structure in its vicinity, are more complicated. Due to the oxygen's high electronegativity it attracts electrons from the surface and therefore decreases the DOS in the metal. The electrons attracted appear as p-wave states in the oxygen, which are below the Fermi level and therefore, do not contribute to the DOS at the Fermi level. Oxygen appears as a depression

for commonly used distances. However, due to the chemisorption of O on Ni, the unfilled, largely delocalized 3s states of O can be populated with Ni electrons. Therefore it appears as a small protrusion for larger distances than 10 Å between tip and sample.

The contrast observed for more complicated adsorbates cannot be explained anymore with the jellium model [26].

There is a large variety of models interpreting STM images. Some of the more advanced models treat the electronic states of the sample and the tip more realistically. This is the base to avoid some of the approximations made to calculate the tunneling current after Tersoff and Hamann. A more realistic electronic structure is, amongst others, often obtained by Density Functional Theory (DFT) [38].

Another improvement is to use different methods to calculate the tunneling current itself instead of the perturbative approach. Such models are based e.g. on a layer Green function formalism where the perturbation in the Hamiltonian due to the adsorbate is solved with a Green's function [39] or the electron scattering quantum chemical approach (ESQC) [40]. Depending on the adsorbate studied, there are different models which simulate the experimental data satisfyingly. Unfortunately, there is no general approach at present that explains the imaging contrast for all systems.

3.2 Molecules

The interpretation of images of molecules, in contrast to adatoms, adds a level of complexity. First, it is not necessarily clear what the observed internal structure of such molecules means. It can reflect the orbitals of the

molecule or the electronic structure of the intramolecular bonds, which is not evidently related to the geometrical structure of the admolecule. Furthermore, molecules can adsorb on different lattice sites of the surface, which in the same image makes the same molecule look different under the exact same conditions like bias, distance, and tip.

A simple, first theoretical attempt to understand an image, proposed by Sautet [26], is the decomposition of the tunneling current: The through space current resulting from the tip - bare surface interaction is weakened in the region of an admolecule, resulting in a lower current. Moreover, there is a through-molecule current due to the tip-molecule interaction, resulting in a higher current. The total current and therefore the real contrast is the superposition of these two contributions.

To use this simple model more qualitatively it is necessary to understand what the contribution of the through-molecule current to the total tunneling current is. There are two main factors: First, a molecular orbital (MO) close to the Fermi level contributes more then a MO far away. However, since the tunneling current resonance has a Lorentzian shape (see Figure 3.3), it's decay depends on $\frac{1}{(\triangle E)^2}$, where $\triangle E$ is the energy difference between Fermi level and the energy of the MO. Second, the strength of the coupling between the MO, the surface and the tip states, which determines the width of the resonance (β). An important aspect for these interactions is the number of nodal planes of the adsorbates electronic states perpendicular to the surface. The more nodes there are and therefore the more localized the electronic state, the less is their contribution to the tunneling current, as a rule of thumb.

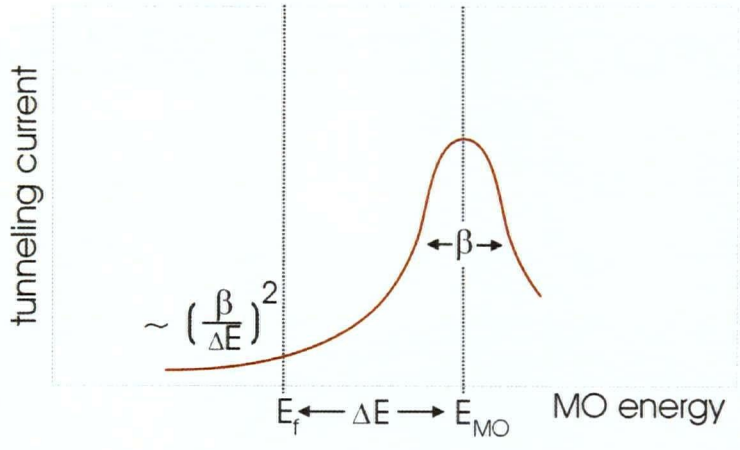

Figure 3.3: Schematic representation of the Lorentzian shaped tunneling current response for a given MO overlapping with its tail the Fermi level after[26]. β is the width of the resonance, determined by the MO-surface and the MO-tip interaction.

This simple model allows a basic understanding of the imaging of CO on Pt (111) [41]. Depending on the adsorption site of CO on Pt(111), CO can be imaged as a protrusion of 0.44 Å sitting on a lattice top site and as a "sombrero" with a central protrusion of 0.14 Å in the very same image. The through-molecular current, contributing to a protrusion, is mainly due to the 5σ MO of CO. The two bonding and anti bonding orbitals, π and π^*, contribute very little to the tunneling current since they are oriented perpendicular to the CO molecule which sits upright on the surface. The O orbitals are supposed to be strongly contracted in the CO molecule and therefore contribute only very little to the 5σ MO. This is an explanation for the small imaging height of 0.44 Å versus the geometrical height of 3 Å of CO on Pt (111). The geometrical height is defined as the distance from the core of the surface atom to the core of the Oxygen of the CO.

The contrast of CO on Cu (111) is even weaker and the molecule appears in the STM image as a depression as observed by several groups [33, 42, 43] including us. A satisfying theoretical interpretation was just presented in 2004 by Nieminen [27, 28, 44], relying on the generalized Green functions approach by Sautet [45]. To analyze the CO images, especially of a CO cluster which was assembled in this work, it is necessary to give a brief introduction into the Green function approach.

Using the Todorov-Pendry approach (TP) [46, 47], the tunneling current between the orbitals of the tip (τ) and the substrate (σ) can be written in the form:

$$j = \frac{2\pi e}{\hbar} \int [f(E) - f(E + eV_b)] Tr[\rho^0_{\sigma'\sigma}(E) T_{\sigma\tau}(E) \rho^0_{\tau\tau}(E) T^{\dagger}_{\tau'\sigma'}(E)] dE. \quad (3.1)$$

Here ρ^0 is the density of states matrix for the system without an adsorbate and T is the Transition Matrix. T can be written in the form $T = V + VG^+V$ where V is the Hamiltonian Matrix for the bare substrate and G^+ is the Green's function for the system with an adsorbate.

That means that the current will be finally proportional to the Transition Matrix T: $I \propto |T|^2$

To get a better physical understanding of the Transition Matrix, Nieminen used the tunneling channel approach, where the T-matrix is decomposed in a localized basis [28]:

$$T_{\sigma\tau} = V_{\sigma\tau} + V_{\sigma\mu} G^+_{\mu\sigma'} V_{\sigma'\tau} + V_{\sigma\mu} G^+_{\mu\nu'} V_{\nu\tau} \quad (3.2)$$

, where the adsorbate orbitals are denoted by μ and ν whereas the tip and

substrate orbitals are σ and τ.

This equation describes three main paths for the tunneling electrons, which are also called the tunneling channels (therefore tunneling channel approach). The first channel $T_1 = V_{\sigma\tau}$ is the *direct through vacuum* channel between the unperturbed tip and substrate states. $T_2 = V_{\sigma\mu}G^+_{\mu\sigma'}V_{\sigma'\tau}$ is the through vacuum channel but with *scattering from the adsorbate*, where different scattering channels can be attributed to the adsorbate orbital μ. The third channel $T_3 = V_{\sigma\mu}G^+_{\mu\nu'}V_{\nu\tau}$ represents the *tunneling through adsorbate* path. To visualize the paths the reader is referred to figure 3.4. It shows a schematic drawing of an adsorbate on a substrate and the tip with the described channels T_1, T_2 and T_3 contributing to the tunneling current. The doted lines represent the Hamiltonian matrix element V, whereas the solid lines represent the Green's function, coupling the adsorbates orbitals to the substrate and tip states.

The advantage of this model is first that it is still physically descriptive and second that it explains how the tunneling current can vary, depending on the contribution of the channels as will be explained in the following.

The contribution T_1 directly from the substrate is in this model always the same and since it is simply the Hamiltonian Matrix,

$$T_1 = V_{\sigma\tau} = \int \phi^*_\sigma(r) H \phi_\tau(r) d^3r \tag{3.3}$$

it is always real. The two other tunneling channels T_2 and T_3 however, include also an imaginary part due to the Green's function G^+, coupling the adsorbate states to the tip and surface states. The real and imaginary part of the Green's function reveal information about the nature of the tunneling

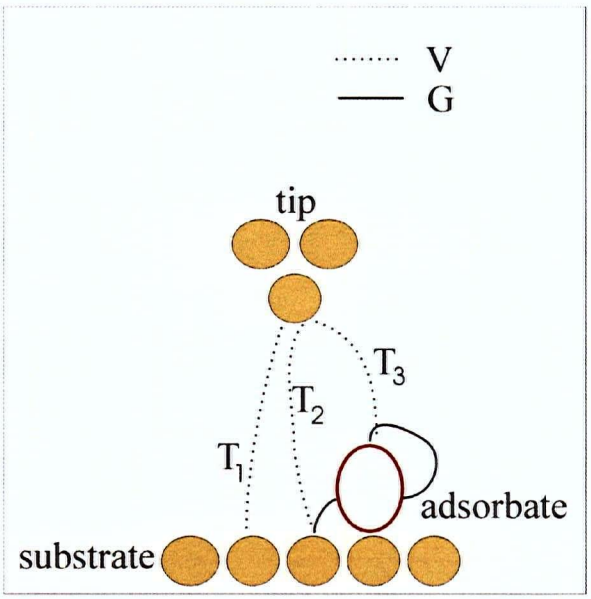

Figure 3.4: Schematic drawing of the tunneling channels T_1, T_2, T_3 in the presence of an adsorbate [27]. The doted lines represent the Hamiltonian matrix element V, whereas the solid lines represent the Green's function, coupling the adsorbate orbitals to the substrate and tip states.

current since the Green's function generally is a response function to an external perturbation.

The imaginary part of the Green's function for example gives the eigen-spectrum of the possible tunneling channels. However, more interesting is the influence of the phase of the Green's function on its real and imaginary part. The matrix elements of a Green's function can be written in terms of its absolute value and an imaginary exponent containing a phase:

$$G^0_{aa} = |G^0_{aa}| \exp^{i\varphi_{aa}} \tag{3.4}$$

where a indicates in this case the adsorbate orbitals and φ the phase. To get an idea on the meaning of the Green's function's phase we look at the simple case of a Green's function for a single atom with one valence electron level E_a:

$$G^0_{aa} = \frac{1}{E - E_a + i\eta} = \frac{\exp^{i\varphi_{aa}}}{\sqrt{(E - E_a)^2 + \eta^2}} \tag{3.5}$$

where η determines the width of the resonance. This leads to

$$\varphi_{aa} = \arctan[-\frac{\eta}{E - E_a}]. \tag{3.6}$$

This tells us two things about the Green's function. First its absolute value is essentially only non zero around the resonance where $E = E_a$ and second that the phase changes from $\varphi_{aa} = \pi$ for energies below resonance over $\varphi_{aa} = -\frac{\pi}{2}$ in resonance to $\varphi_{aa} = 0$ above the resonance.

The important point here is to realize the possibility of a change in phase, which manifests itself in a change of the sign in front of the real and imaginary

part of the Green's function and therewith in a change of the sign of the single transition matrices T_2 and T_3.

For a diatomic molecule the Green's function matrix elements become more complicated, as discussed in detail in reference [28]. However, the principle is the same: Around resonances the phase can change but also between an energy gap of two energetically following molecular orbitals (MO), due to different paths through the molecule. This leads again to different signs in front of the Transition Matrices T_2 and T_3, which results, recalling $T = T_1 + T_2 + T_3$, in constructive or destructive interference of the tunneling currents.

Using a hypothetical example: T_3 has a similar amplitude than T_1, let's say $0.7T_1$ but due to the phase difference compared to T_1 it is -$0.7T_1$ and T_2 contributes with $0.2T_1$ we get a total $T = 0.5T_1$. Since the current is proportional to the square of T, $I \propto T^2$, the current directly over the adsorbate would be only a quarter of the bare substrate current . Therefore the adsorbate would appear as a depression.

To sum this model up: In the presence of an adsorbate there are several tunneling channels and therefore several tunneling currents which contribute to the total tunneling current. These different currents have a certain amplitude as well as a phase which can lead to destructive or constructive interference. The phase depends on the tunneling path of the electron and its energy compared to the energy of the adsorbate's orbitals. This model provides a fairly descriptive way to interpret the imaging of simple systems like CO on Cu [27, 28, 44] as I will show in the analysis part in Chapter 4.

Interpreting images of larger and more complex molecules involves so-

phisticated modeling and cannot be explained qualitatively with any of the presented models. As further literature the review paper by Sautet [26] is recommended.

Chapter 4

Experimental setup

Measurements on single adsorbates with a Scanning Tunneling Microscope need perfectly clean and well defined conditions. This requires a sophisticated experimental setup, which will be described in this chapter. The setup combines home-built and commercial components.

To meet such well defined conditions it is necessary to work under Ultra High Vacuum (UHV) and to reduce any form of vibrational interference to a minimum. For manipulation experiments it is furthermore important to work at low temperatures, where the studied adsorbates do not diffuse on the substrate.

In the following I will describe the UHV system and the devices used for the sample preparation. The second section addresses the specifics of the STM. In the third part the tip and sample preparation are described and in the last part the calibration of the STM will be discussed.

4.1 UHV chamber

The chamber is divided into a preparation chamber and a STM chamber, which is divided by a gate valve. The first chamber contains all the preparation instruments and the second chamber the STM and the cryostat. A manipulator is used to transfer the sample between the two chambers.

To avoid contamination of the sample during preparation and measure-

ment a base pressure of 10^{-10} mbar is needed. Therefore a combination of different pump stages is used. The pressure is measured with Pfeiffer cold cathodes.

The first pump stage is the fore vacuum, where a dry membrane pump from Pfeiffer is used to avoid backflow contamination. This pump achieves a pressure of 1 mbar, which is sufficient for the second pump stage, a Pfeiffer Turbo pump with magnetic bearings to reduce vibrational interference. This 300 l/s turbo pump reaches a pressure of 10^{-10} mbar in the chamber. Parallel to the large turbo pump a smaller 50 l/s turbo pump is connected to the fore vacuum. This pump supplies the rotary motion feed through of the manipulator with a pressure of 10^{-7} mbar.

Both chambers are additionally pumped by an ion pump each. These passive pumps decrease the pressure by half a magnitude but predominantly ensure a steady low pressure. The chamber where the sample preparation takes place has an additional titanium sublimation pump. A titanium film is evaporated on a panel cooled with liquid nitrogen. The titanium binds most of the oncoming particles for the duration of it's low temperature or until the film is saturated. It lowers the pressure to 1×10^{-10} mbar for about 2 hours and binds especially the hydrogen and is used before a sample preparation.

The chamber containing the STM includes a bath cryostat, which acts like a large cryo pump. The cryostat's temperature shields have a temperature of 5 K and lead to the condensation of particles. This yields to a very low pressure in the STM between the radiation shields that is not directly measured by a gauge. The only indication for the pressure in the STM is the time a sample stays uncontaminated which is in our case two to three weeks.

To achieve a better pressure the whole UHV system is baked out. Therefore, an insulated aluminum chamber was built. The heating is carried out by a combination of ceramic heaters and 10 cm wide heating bands around the pump flanges. The temperature is measured with K-type thermo elements and controlled by Watlow temperature controllers.

For an overview over the whole setup, figure 4.1 shows the UHV chamber including the attached instruments and pumps on pneumatic vibration isolators.

The UHV-setup, as mentioned, is divided into two chambers, separated by a built-in VAT gate valve. In the first chamber the samples are prepared, and the second contains the STM and the bath cryostat. The whole chamber was modified from the original CreaTec `http://vts-createc.com/` design to satisfy our specific needs by Agustin Schiffrin, a PhD student in our group.

The preparation chamber contains a sample storage, the standard sample preparation devices as will be described above and a Low-Energy Electron Diffractometer (LEED) to analyze the sample surface structure. The single crystal substrates used for this work were Ag (111), Cu (111) and Cu (110). Each substrate was mounted on a separate sample holder shown in figure 4.2. Below the sample a button heater and a thermocouple are mounted. Both can be actuated through electronic contacts. The button heater allows to anneal the sample up to 800° C.

For the sample preparation the following devices were mounted on the chamber:

An argon ion gun to clean the substrate's surface and the mentioned button heater on the sample holder to smoothen out the surface. For the

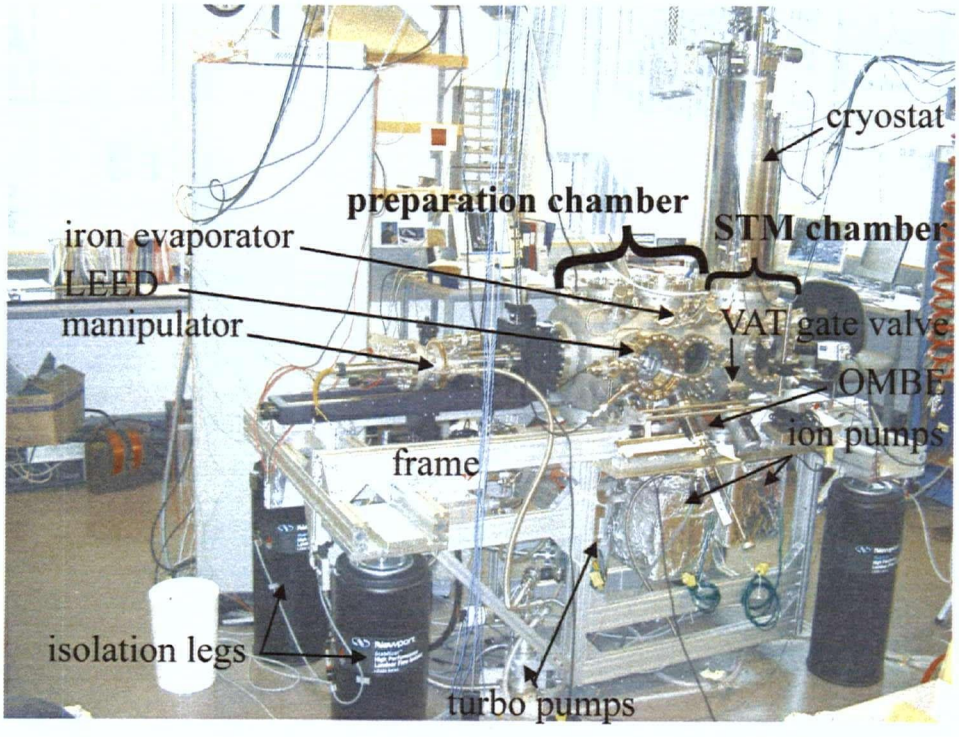

Figure 4.1: Overview of the experimental setup. The UHV chamber is divided into two parts separated by a built-in VAT gate valve. The left chamber contains the devices for the sample preparation. The right chamber accommodates the STM and the cryostat.

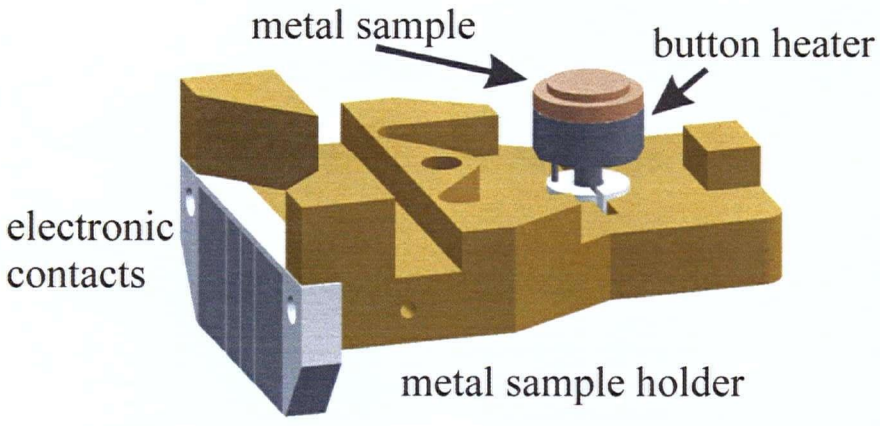

Figure 4.2: Schematic drawing of the sample holder after Crea Tec. The button heater and a not shown thermocouple can be actuated by the electronic contacts. Any of these contacts can be used in the STM to apply the bias voltage between tip and sample.

deposition of adsorbates an Organic Molecular Beam Evaporator (OMBE), a resistive iron evaporator and a CO gas intake are available. A Low-Energy Electron Diffractometer (LEED) is attached to do a first sample surface characterization.

To move the sample holder between the preparation devices and finally to transfer the sample into the STM a manipulator is used.

The OMBE was purchased from Kentax `www.kentax.de` and can evaporate up to four different molecules. Each molecules is placed in a crucible which can be heated up separately by a filament. The evaporated dose is controlled by the temperature and the evaporation time, controlled by a shutter. The setup allows to evaporate up to three molecules in parallel. The OMBE is separated from the preparation chamber via a gate valve and is pumped independently to allow the exchange of molecules without breaking the vac-

uum.

The CO-gas inlet is controlled by a leak valve.

A VAB manipulator with four motion degrees of freedom is used, shown in the overview image of the UHV chamber 4.1. The manipulator head, and therewith the sample, can be cooled by a flow cryostat to 50 K. Electrical contacts on the head allow the control of the button heater and the thermocouple of the sample holder. The sample holder is coupled to the manipulator via an externally accessible T piece.

For a characterization of the substrates surface quality the LEED is used. The basic principle is very much the same then x-ray spectroscopy with the modification of only a two dimensional diffracting surface. Due to the low energy (20 - 200 eV) the electrons penetrate only a few atomic layers into the solid, so that the diffraction pattern is mainly determined by the surface atoms.

The electrons are elastically scattered back towards a phosphorus screen where the interference pattern can be observed. The interference pattern will show varying intensities between the peaks characterizing the surface structure.

4.2 STM

The main instrument of the whole setup is the Scanning Tunneling Microscope. It is placed in the second chamber, which has a double walled bath cryostat mounted on top of it. A schematic drawing of the cryostat is shown in figure 4.3. The outer reservoir is filled with liquid nitrogen, the central

one with liquid helium. The STM is attached by springs at the bottom of the cryostat and surrounded by radiation shields. Shutters in the radiation shields allow the sample transfer into the STM and in situ evaporation. For the sample transfer, and to cool the STM head down to 5 K it is pulled via a cable onto the base plate of the inner radiation shield. The radiation shields have furthermore two small windows for optical access. During the measurement the STM hangs freely from the springs to reduce vibrational noise. The equilibrium temperature in the hanging position after cooling the STM to 5 K is 10 K.

The STM used here is a commercially available version (CreaTec) produced after a home built design developed by G. Meyer at the Freie Universität Berlin. It is a Besocke beetle type STM which consists of three outer and one inner piezo element, shown in figure 4.4.

These piezos are tube piezos which can move in all three directions. The synchronized outer piezos have sapphire spheres mounted on top of them. On the sapphires sits an approach ring which holds in its center the fourth piezo, with the STM tip on its end. The approach ring has built-in ramps of 2 degrees so that the outer piezos can move the tip via a moment of inertia drive for the coarse approach towards the sample. In the scanning mode, both central piezo and/or outer piezos can be used. In this work the z-direction was controlled by the central piezo and the x-and y-direction by the outer piezos. This has the advantage that the scan direction in the plane compared to the crystal axis does not change between preparations since the three outer piezos are fixed compared to the sample holder orientation and furthermore, x,y and z are decoupled from each other

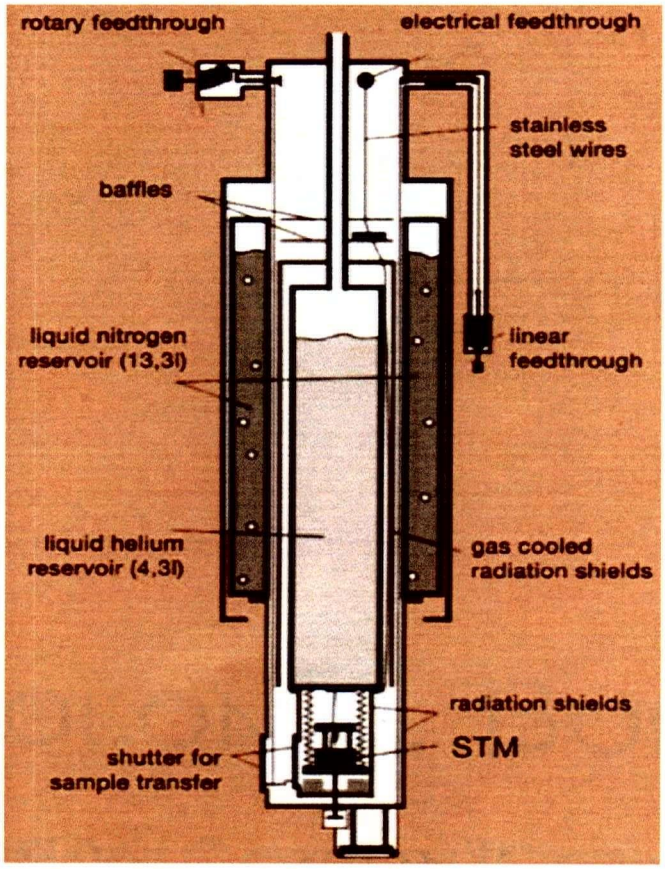

Figure 4.3: Drawing of the cryostat after CreaTec. The double walled cryostat cools the STM and a temperature shield, which keeps the STM constant at a low temperature. The STM itself hangs from the bottom of the cryostat on springs to reduce vibrational noise.

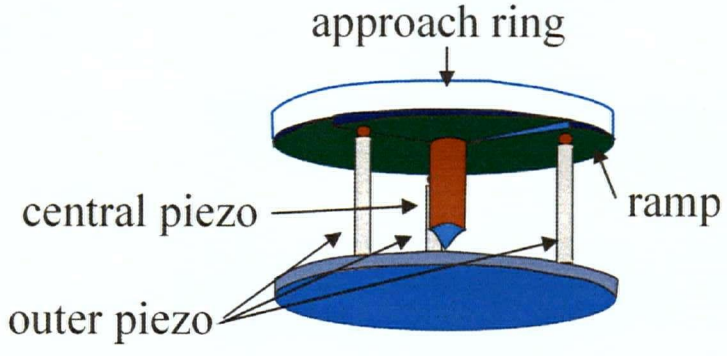

Figure 4.4: Schematic drawing of a Besocke type STM. The three outer piezos rotate the approach ring and the inner piezo holds the tip. The scanning can be done by both the inner or the synchronized outer piezos. The drawing dimensions of the piezos are not in scale for reasons of overview.

To get an additional overview the STM is schematically shown in figure 4.5. As already mentioned the STM hangs on steel springs from the bottom of the cryostat for vibrational isolation purposes. To additionally damp vibrational noise, an eddy-current brake is used, sitting at the bottom of the STM indicated with the magnet opposing the edge of the baseplate.

The STM is operated via a digital-signal-processor (DSP), which is controlled by a program on a regular PC. The advantage is, that the remaining electronics is fairly straightforward: A current amplifier, a high-voltage amplifier for the piezos and a dividing amplifier for the sample-tip bias.

The tunneling current is amplified and then fed through an analogue-digital (A/D)-converter into the DSP. The DSP controls the piezos through four D/A-converters via the high-voltage amplifier. The working frequency for the DSP is 50 kHz.

The DSP makes it possible to control a wide range of applications with the PC program. Apart of several scan modi, there are different manipulation,

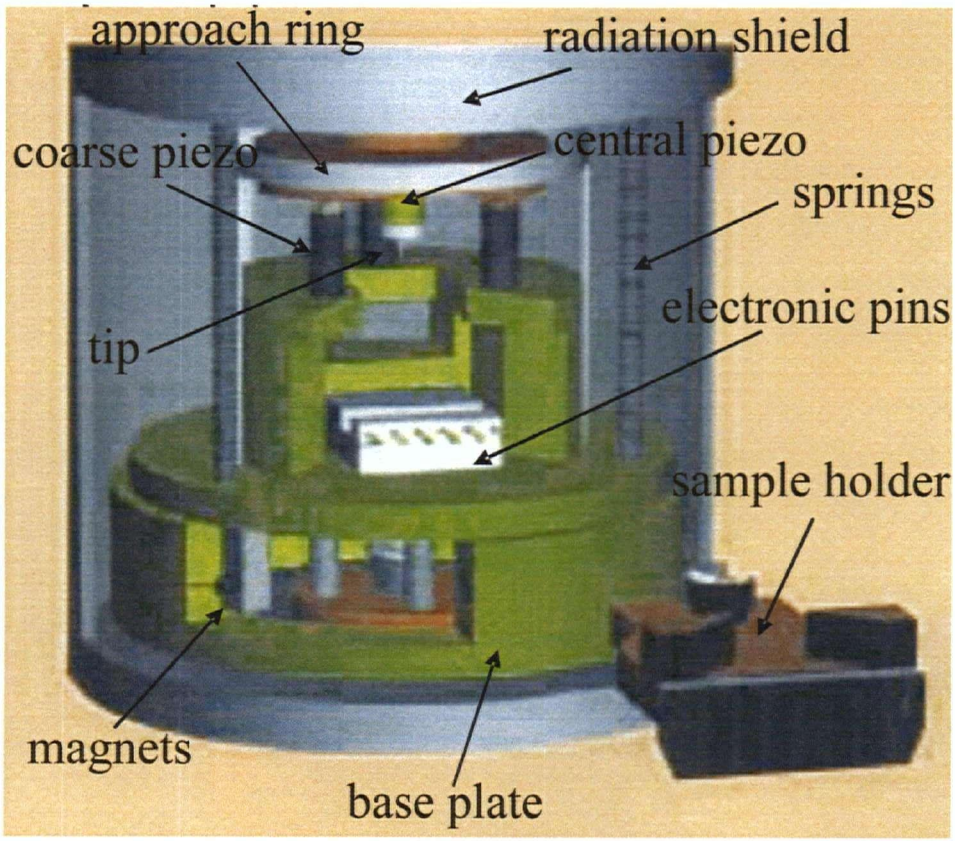

Figure 4.5: Overview drawing of the STM inside the radiation shield by Crea Tec. The electronic pins are the counterpiece to the electronic contacts on the sample holder to apply the bias between tip and sample. The magnets orientated towards the base plate act as eddy-current brakes to reduce vibrational noise.

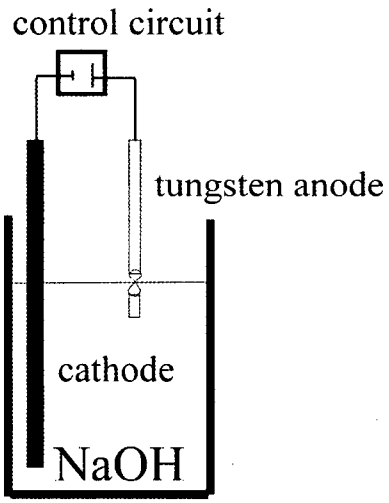

Figure 4.6: Schematic drawing of the etching setup for STM tips. The tungsten wire is etched the most at the meniscus of the NaOH around the wire and forms therewith very sharp tips

spectroscopy and tip-forming modi.

4.3 Tip and sample preparation

The most important part of the STM is the tip. Initially the tip is formed by electro-chemical etching, where a tungsten wire is placed into a 2-molar aqueous sodium hydroxide (NaOH) solution shown in figure 4.6. The anode is an aluminum bar and the cathode is the actual tungsten wire. The etching process is strongest at the meniscus around the wire, where it penetrates the surface of the solution. Therewith it is possible to form sharp tips [48]. The chemical reaction is

$$W(s) + 8OH^- \rightarrow WO_2^{-2} + 4H_2O + 6e^- \tag{4.1}$$

After the etching process the remaining oxides are removed with hydrofluoric acid and finally the tip is neutralized with distilled water. In the chamber the tip is sputtered and transferred into the STM via the manipulator on a special tip sample holder. The tip can be additionally "formed" in the STM by driving it controlled by the program four to five atomic layers into the sample. The tip forming is a very common procedure since the tip apex changes very frequently but only possible with metal substrates.

The sample preparation is a standard procedure in surface science. The cleaning process is a combination of bombarding the substrate with argon ions, called sputtering, and annealing. This combination is referred to as one cleaning cycle. The base pressure before the cleaning is ideally in the order of 10^{-10} mbar. The ion bombardment sweeps away atomic and molecular contamination and the annealing of the substrate evens out the surface.

For the sputtering argon is left into the chamber through a leak valve until the pressure in the chamber is constant $2 \cdot 10^{-5}$ mbar. The substrate is placed in front of the ion gun so that the ionized argon atoms incidence normally on the substrate. The ions are typically accelerated with a bias of 1 kV. The current of ions hitting the substrate is approximately $5\,\mu$A . After the sputtering the leak valve is closed obtaining again a base pressure of 10^{-10} mbar.

The remaining craters in the substrate due to the bombardment are smoothed out by annealing the substrate. Cu (111) is annealed at 800 K and Ag (111) at 750 K. Due to the high mobility of the surface atoms the craters are compensated to energetically more favorable smooth surface configurations like flat terrace planes in the case of the substrates used for this

work.

The first cleaning cycle used in this work was a combination of 30 minutes sputtering and 10 minutes annealing. The following cycles were 20 minutes sputtering and 10 minutes annealing. Usually there were three to four cycles done, depending on the initial state of the substrate.

After the substrate has atomically flat terraces, adsorbates can be placed on the surface with the described deposition devices attached to the preparation chamber.

The sample is then cooled with the manipulator to 130 K before it is transferred into the STM. To cool the sample in the STM to 5 K it takes three to four hours. For the measurement the STM is released from the base plate and is hanging free from the springs which are then the only thermal contact to the bath cryostat.

4.4 Calibration

Measuring the correct distances and height differences of a substrate lattice or adsorbate layer is crucial for the correct interpretation of STM images. The extension of the piezo elements is strongly dependent on the temperature. At 300 K the sensitivity of the piezo in lateral direction was determined to be 100 Å/V whereas at 18 K it is reduced to 16 Å/V. In the vertical direction at room temperature the expansion is 60 Å/V and at 18 K only 7.5 Å/V. This means that the STM has to be calibrated for every temperature. For our studies the STM is used mostly at 18 K and in rare cases at room temperature. Therefore the STM was calibrated at these temperatures.

For the calibration Ag(111) and Cu(111) samples were used because

of their well-known lattice constants and monoatomic step heights. The preparation of these substrates was done as described in the previous section.

First the STM was calibrated at room temperature with Ag (111). The theoretical monoatomic step height for Ag (111) is 2.3 Å and the surface lattice constant is 2.9 Å. This values were achieved with a vertical piezo constant of 60 Å/V and a lateral piezo constant of 100 Å/V at room temperature. The length ratio between the different lattice constants, 60° oriented to each other, was one which perfectly agrees with the theoretical ratio. Figure 4.8 shows atomic resolution on Ag (111).

Then the STM was calibrated at 18 K. The vertical piezo constant was calibrated by imaging several atomic steps on a Cu 111) surface at 18 K. Figure 4.7 shows a Cu (111) surface with several terrace steps. The line scan shows monoatomic step heights of 2.1 Å corresponding to the theoretical value with a piezo constant of 7.5 Å/V. To get a statistical value for the step height, 10 different line scans at different positions were taken. Since the sensitivity of the piezos in the different directions changes with the same ratio in temperature this method can be used also for an approximate lateral calibration in case atomic resolution is not possible.

The lateral calibration was done by imaging the atomic lattice of Cu (111), shown in figure 4.8. The theoretical value for the surface lattice constant of Cu (111) is 2.55 Å and the ratio between the length of the lattice vectors is 1. Experimentally these values were achieved with a lateral piezo constant of 16 Å/V. The ratio of the lattice vectors, was measured to be 1, independent of the piezo constant.

The measured angle between the lattice vectors were in both cases of

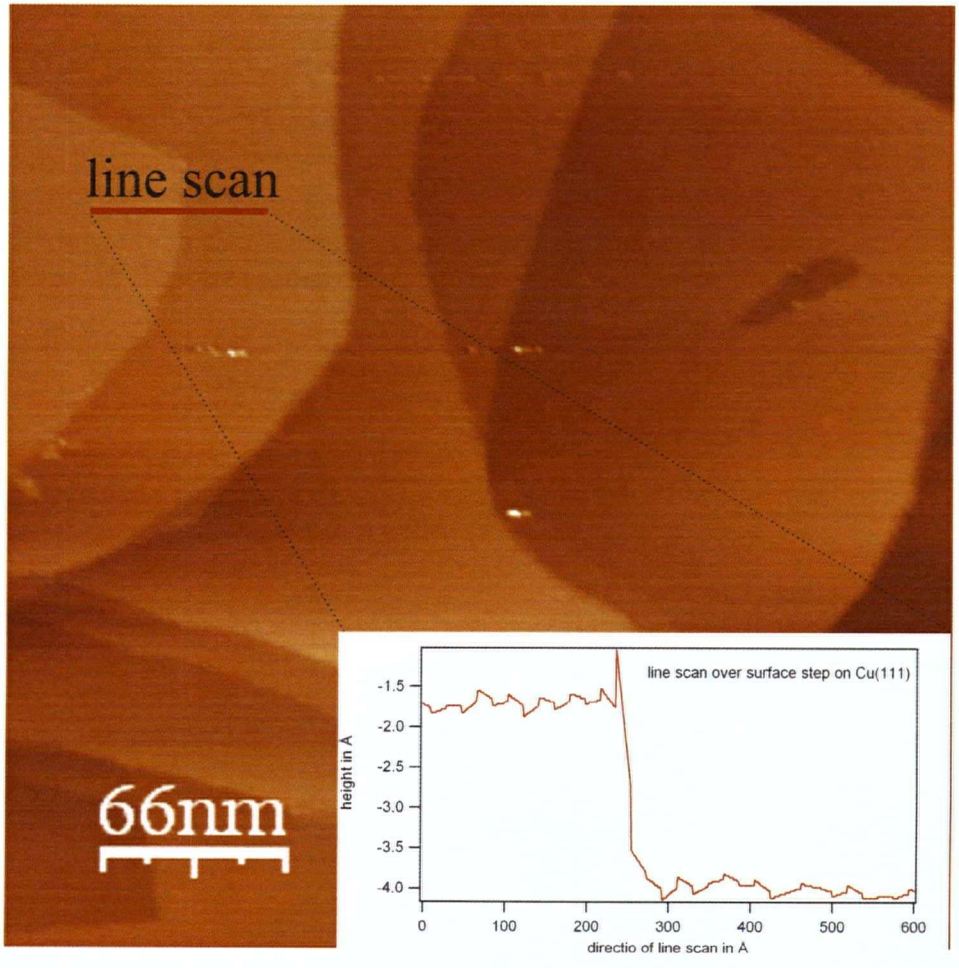

Figure 4.7: Overview image of a Cu(111) surface with several monoatomic steps at 18 K. The red line shows a line scan over an atomic step with a height of 2.2 Å. This image was used to calibrate the piezo constant in z-direction. The bias used was 1 V and the tunneling current was 1.8 nA.

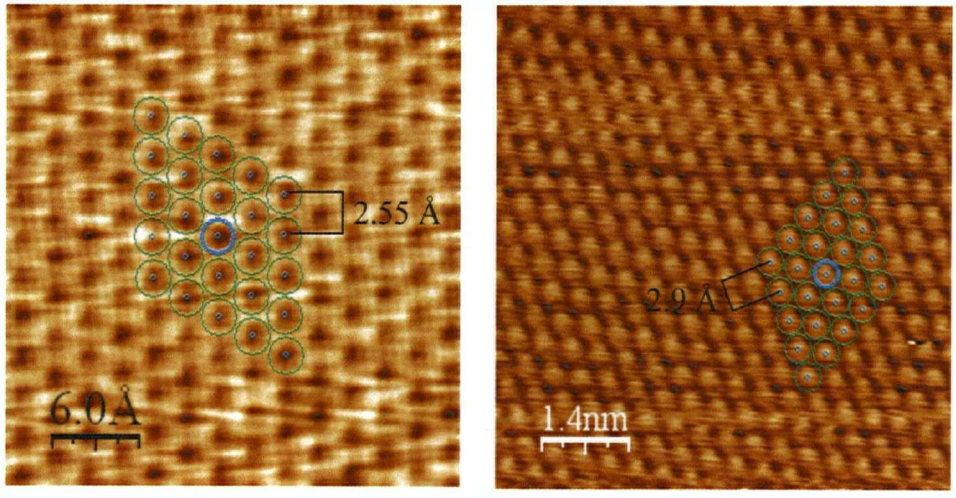

Figure 4.8: Atomic resolution of a) Cu(111) and b) Ag (111) with an underlying lattice with the lattice constant of 2.55 Å for Cu (111) and 2.9 Å for Ag (111). The image of the Cu was taken at 18 K with an applied bias of 27 mV and a tunneling current of 0.65 nA. The Ag image was taken at room temperature with an applied bias of 89 mV and a tunneling current of 1.1 nA.

Ag (111) and Cu (111) $60 \pm 1°$, which corresponds perfectly to the symmetry of the surface.

After the calibration of the piezo constants at room temperature and at 18 K, dimensions on surfaces at the calibrated temperatures can be determined with an accuracy of 10%. This uncertainty is due to the hysteresis of the piezo where the theoretical full extension is reached after a very long time. This leads to different distance measurements at the same temperature due to different scan speeds and varying image sizes. The latter cause can lead in case of images larger then 500 by 500 nm to distortions at the margin of the image. To achieve a higher accuracy, one has to calibrate the corresponding image itself.

The resolution perpendicular to the surface depends strongly on the noise.

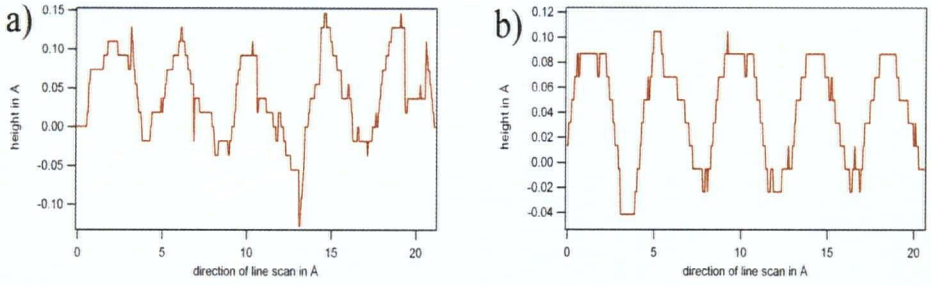

Figure 4.9: Line scan over 5 silver atoms. Figure a) shows the raw data where the spikes can be interpreted as noise of 0.05 Å. Figure b) shows the same line scan over the same atoms after filtering the image by averaging over neighboring pixels. There the maximum noise is 0.02 Å.

In the case of atomic resolution of Ag (111) a line scan was performed over 5 atoms, shown in figure 4.9 a) and b). Figure a) shows the raw data where the noise level is approximately 0.05 Å which is therewith the resolution limit. In figure b) the same scan over the same atoms was performed after applying a low pass filter, where the data are averaged over neighboring pixels. This reduced the noise to 0.02 Å.

After the calibration of the instrument it's stability and sensitivity could be tested by imaging standing surface states on Cu (111). Surface states are electrons in a solid restricted to a region close to the surface (typically a few atomic layers deep). These surface states can be scattered at impurities on the surface or monoatomic steps forming standing waves around the scatterers. These standing waves are very subtle and change the DOS at the Fermi level only a few percent. This corresponds to an apparent height in the STM image of a very few pm. This phenomena can be best observed at low temperatures since there are not many contributions of different energies. However, to image standing waves a very stable setup is necessary.

Since the modulation of the DOS is very small the applied bias must be small as well to integrate only over a few states to resolve the modulation. The wavelength of these standing waves on Cu (111) is measured to be 15 Å with an amplitude of 0.03 Å [49].

Figure 4.10 shows an image of Cu (111) at 18 K with impurities on the surface. Around these impurities a modulation of the surface can be observed, interfering with each other in the region where several impurities sit next to each other. The applied bias voltage used was 35 mV and the tunneling current 2 nA. The line scan over the indicated impurity reveals the standing waves around the central deeper impurity. The wavelength of these standing wave was 15 Å and the amplitude 0.05 Å.

With the surfaces imaged for the calibration and the observation of standing waves to test the sensitivity and stability, the new LT STM demonstrated a promising performance. With this stability the new instrument can be used at low temperature to do spectroscopy experiments at single molecules or atoms.

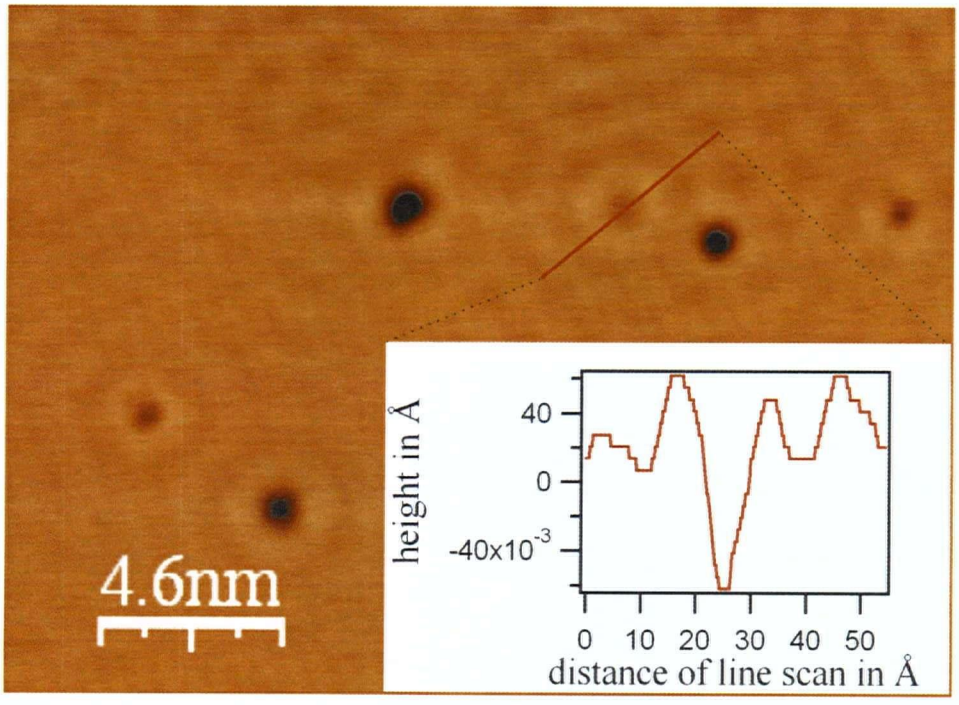

Figure 4.10: Standing waves of surface state electrons on Cu(111) scattered by impurities at 18 K. The applied bias voltage used was 35 mV and the tunneling current 2 nA. In the line scan across the indicated impurity the wavelength and amplitude of the standing waves can be observed. The central deepest depression is the impurity itself.

Chapter 5

CO imaging and writing with single molecules

Determining the precise absorption sites of adsorbates on a surface lattice and manipulating them are the starting point to investigate chemical reactions on surfaces as well as self-organized growth processes which is interesting for both basic and applied research.

The research with the here described LT-STM will focus in the near future on the physical properties and dynamics of self-assembled nanostructures. To investigate the most basic growth processes it is important to understand how adsorbates link to each other and how stable their bonds are. Therefore we decided to test the performance and manipulation abilities of the new STM using a simple system: CO on Cu [50, 51, 52, 53]. This provides the advantage that basic imaging and manipulation parameters are known. Another interesting aspect is the theoretical data interpretation . In this work we demonstrate, that the most recent imaging theory by Nieminen [44] can explain the resolution of single CO molecules and dimers, but does not fully explain the features observed for clusters of CO. Last, it was demonstrated that with the LT-STM setup it is possible to arrange CO molecules on Cu to any structure by writing the "smallest UBC ever". Furthermore it was possible to optimize the manipulation parameters to speed up molecular manipulation.

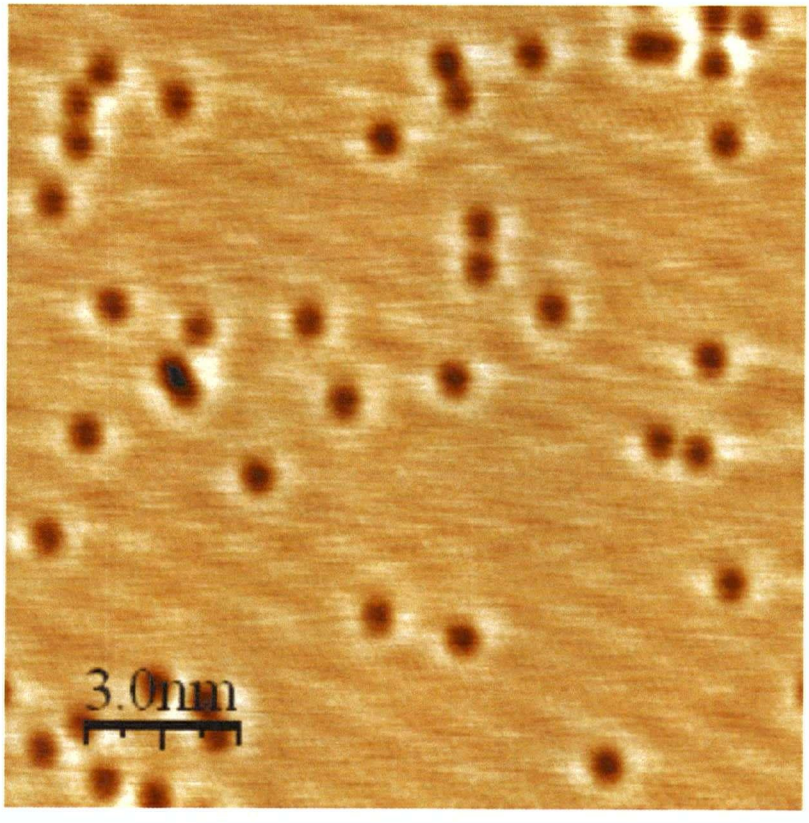

Figure 5.1: Image of CO molecules on Cu (111) at 18 K. The bias used was 0.65 V and the tunneling current was 0.56 nA. CO appears as a depression.

5.1 Imaging CO

The preparation of the atomically clean Cu(111) substrate was achieved as described in chapter 3.3. After the sample was placed in the STM and cooled down, CO gas was dosed into the chamber through a leak valve. The dose of the CO gas was 0.5 L (where 1 L = 1.36 $10^{-}6$ mbar/sec) in both chambers to cover a small fraction of the copper substrate with CO molecules. The coverage of CO molecules was approximately 0.5% as shown in image 5.1.

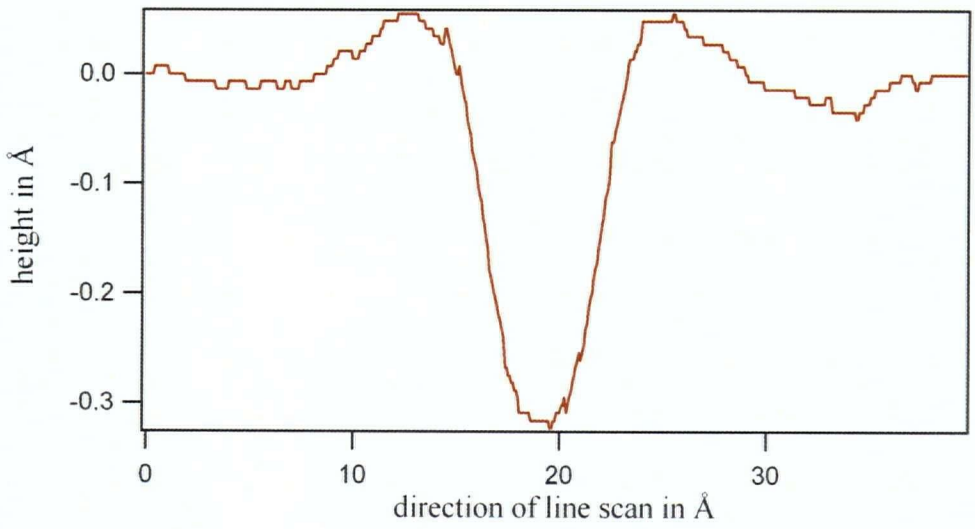

Figure 5.2: Line scan over a CO molecule. At the position of the CO the depression is 0.3 Å deep and 10Å wide.

To image and to manipulate it is important that the CO molecules do not thermally move. Their binding energy on Copper is 0.5 eV. The diffusion energy must therefore be lower, but in the literature a specific value could not be found. Since the diffusion has exponential behavior $D = D_0 e^{-\frac{E_D}{kT}}$ it is difficult to determine a cut off-energy. However, Bartels [54] did not observe diffusion up to 40 K. Therefore the sample was cooled to 18 K equilibrium temperature to keep the CO molecules from diffusing.

Image 5.1 shows that the CO molecules appear as a depression. A line scan over a single CO molecule (fig. 5.2) demonstrates the shape of its contrast in form of a depression, which is approximately 0.3 Å deep and 10 Å wide.

The graphs in figure 5.3 and figure 5.4 show the dependence of width

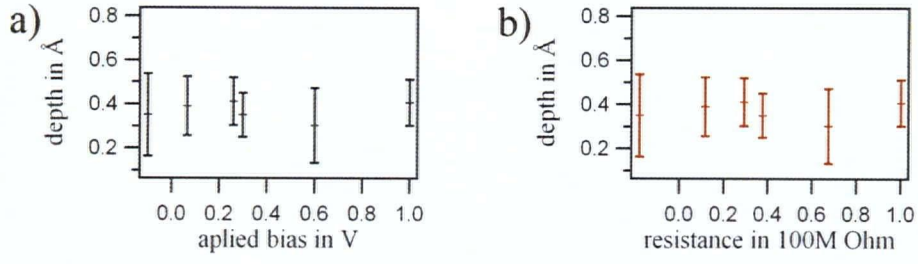

Figure 5.3: a) Shows the depth of the CO depression, depending on the applied bias. b) Shows the depth versus the tunneling resistance. The error bars are a combination of the standard deviation of the sample volume used for each data point and the average noise in the image.

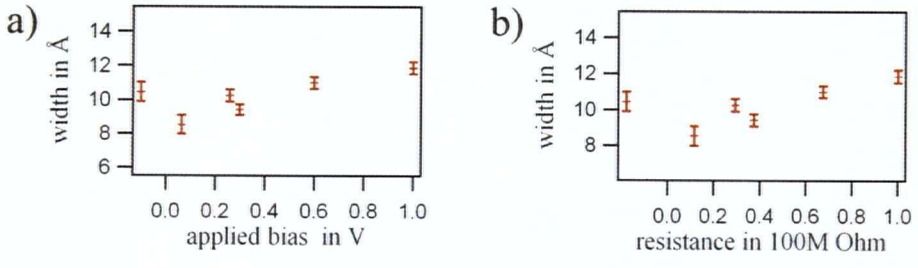

Figure 5.4: a) Shows the width of the CO depression, depending on the applied bias. b) Shows the width versus the tunneling resistance. The error bars are the standard deviation of the sample volume used for each data point.

and depth on voltage and resistance, respectively. It can be seen that the form, depth and width did not depend on the applied bias or the tunneling resistance, in agreement with earlier observations [33].

Both, width and depth were measured on different images with varying bias voltages and tunneling currents but also with changing tip conditions. In each image line scans over 5 different molecules were taken to determine an average depth and width. The error bars in the graphs are a combination of the standard deviation of the averaged line scans and the average noise

of the image. Due to the size of errors as well as the small sample volume, it has to be noted that the statistics are not good enough to draw final conclusions. The fact that the appearance did not change although the tip condition varied, which has an important influence on the image, supports the theses of independent appearance of CO molecules on copper.

The bias-independent appearance of CO molecules on Cu can be explained with a simple symmetry argument. The molecules sit on top of a Cu atom [55] as schematically shown in figure 5.5 a). In the same figure the CO's highest occupied molecular orbital (HOMO) 5σ is illustrated, which contributes to the tunneling current. The energetically next higher orbital ($2\pi^\star$) is the lowest unoccupied molecular orbital (LUMO), which is schematically drawn in figure 5.5 b. Between the LUMO and the HOMO is a large energy gap of 6.9 eV [56] in the gas phase. Once the CO is adsorbed, the energy gap is reduced [56] but still considerably large. Therefore the LUMO is expected to contribute to the tunneling current only for high bias voltages. The main reason why the $2\pi^\star$ orbital is contributing only very little to the tunneling current is its localization. Figure 5.5 b) shows the schematic drawing of the localization of the $2\pi^\star$ orbital with two nodes perpendicular to the surface. The assumed s-wave of the tip does not overlap with the $2\pi^\star$ of the CO molecule and does therefore not contribute to the tunneling current. This means that by applying a larger bias we do not integrate over more states or in terms of the Green's function approach there are not more tunneling channels opened and therefore the appearance of the CO molecules is independent of the applied bias. The same argument applies when the bias is reversed, where the same orbitals mediate the current as before.

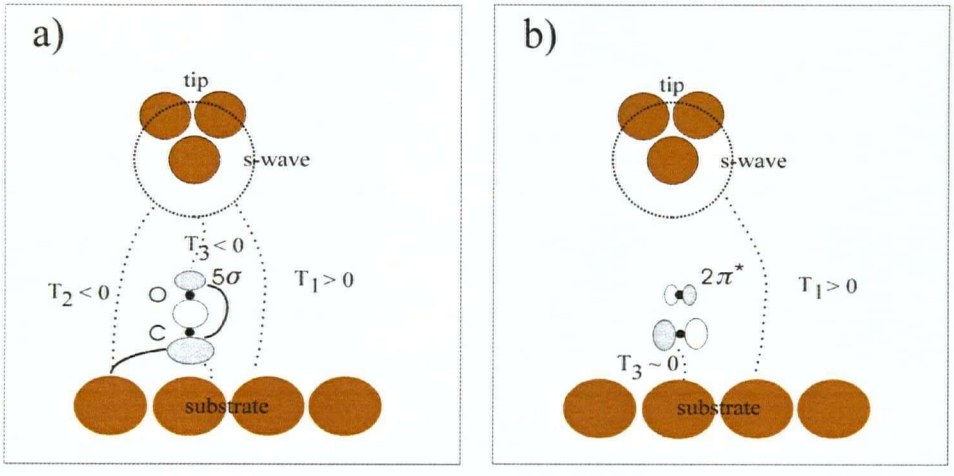

Figure 5.5: a) Shows the LUMO of the CO molecules and the different tunneling paths. b) Shows the HOMO of the CO molecule. In this case, there is due to the antisymmetry no contribution to the tunneling current.

After understanding why the appearance does not depend on the bias, the imaging of CO as a depression has to be explained. To do this the Green's function approach as introduced in chapter 3 is the best suited.

Recalling chapter 3 there are different tunneling channels contributing to the tunneling current which are illustrated in figure 5.5. The tunneling matrix T containing the different tunneling channels $T = \sum_{i=1}^{N} T_i$ is proportional to the tunneling current: $I \propto |T|^2$

Using a bare metal tip to image CO on copper, the transition matrix T is composed of a sum of three different tunneling channels, $T = T_1 + T_2 + T_3$. T_1 is the direct substrate-tip through vacuum channel, T_2 the channel where the tunneling electrons are scattered at the adsorbates orbitals and T_3 the through adsorbate channel [28]. As explained in chapter 3 the different tunneling currents can have different amplitudes as well as phases with respect

to each other.

T_1 is fairly simple to calculate since it is just the integral over the unperturbed Hamiltonian. The tunneling channel T_2 which scatters off the adsorbate 5σ orbital obtains a phase shift of π compared to T_1. The third channel T_3 contributing to the tunneling current goes through the CO molecule itself. The contributing CO orbital is again the 5σ. Electrons of the Cu bulk material with an energy resonating with the 5σ orbital hop into the CO and from there tunnel into the tip (see figure 5.5 a)). Therefore the through molecule current has a phase shift of π compared to the direct through vacuum current as well. This phase shift appears as the opposite sign in front the transitional matrix elements T_2 and T_3 compared to T_1. The $2\pi^\star$ orbital does not open additional tunneling channels due to the already explained symmetry argument.

Nieminen [28] showed that T_2 and T_3 can be calculated in terms of T_1: $T_2 = (-0.19 - i0.15)T_1$ and $T_3 = (-0.59 - i0.66)T_1$. Since $I \propto |T|^2 = |T_1+T_2+T_3|^2$, he found $T^2 = 0.31T_1^2$. This is obviously smaller then the bare substrate tunneling current contribution T_1^2 and therefore CO is observed as a depression.

Niemenen furthermore showed that the phase itself does not change for the electron energy passing the first resonance through the band gap until it passes the second resonance. This explains the possibility of a switch in the phase shift between the energy gap leading to a change in the interference of the channels leading to a change in the contrast.

The destructive interference of T_2 and T_3 are strongest directly over the CO molecule. Their contribution to the tunneling current decreases expo-

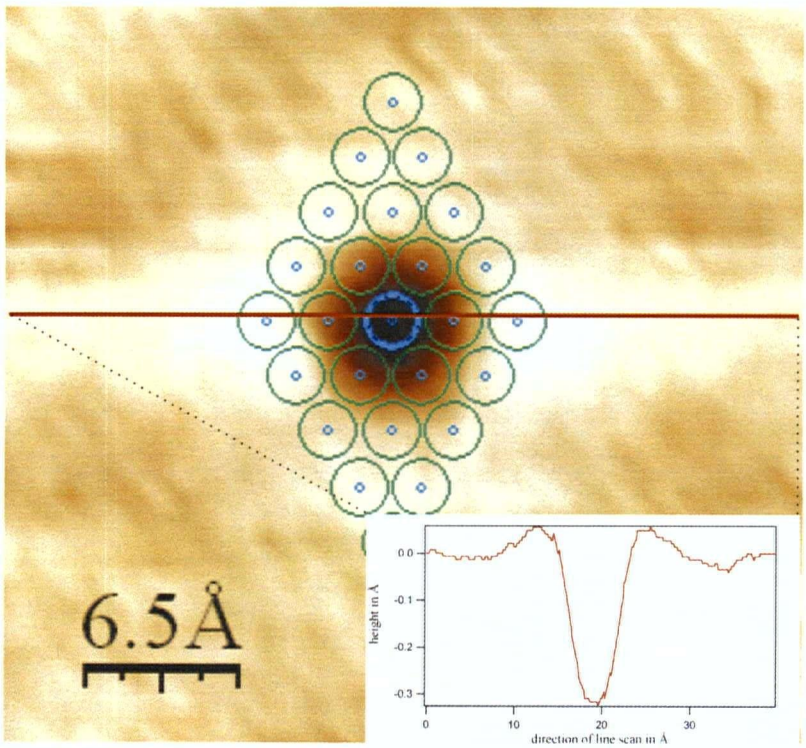

Figure 5.6: Image of a single CO molecule on Cu(111) at 18 K taken with a bias of 0.3 V and a tunneling current of 8 nA. The lattice underneath represents the Cu (111)lattice and the red line shows the direction of the line scan, demonstrating the exponential decay of T_2 and T_3.

nentially with lateral distance to the adsorbate. This can best be seen in the line scan over an imaged CO molecule in figure 5.2 and figure 5.6. The width of the depression is about 10 Å which means that the influence of T_2 and T_3 decays after 5 Å. To compare the size of the depression with the lattice sites of the Cu (111) crystal a grid representing the Cu atoms is superimposed in figure 5.6.

The image of a cluster of CO molecules can be explained for the most part by what was learned about imaging a single CO molecule. Figure 5.7

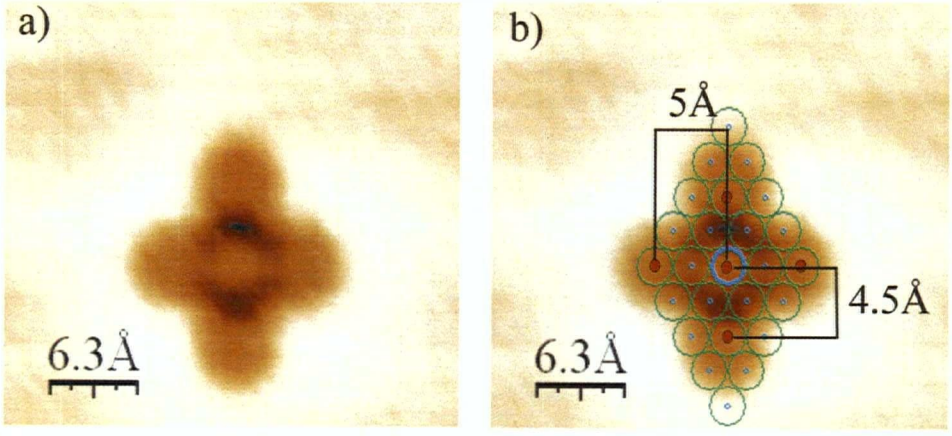

Figure 5.7: a) Shows a cluster of 5 CO molecules on Cu(111) forming a plus sign. The image was taken with a bias of 0.3 V and a tunneling current of 8nA at 18 K. b) Shows the underlying Cu (111) lattice where the red marks indicate where the CO molecules sit.

a) and b) show an image of a CO cluster containing 5 CO molecules forming a plus sign. In Figure 5.7 b) the plus sign has the Cu (111) lattice superimposed. The red marks indicate the adsorption sites of the CO molecules on the next nearest neighbors of the Cu lattice. For further simplification in the discussion I will refer to the top, central and bottom molecule as the vertical aligned molecules, whereas the left, central and right COs as the horizontal aligned molecules. The distance between left and right CO molecule from the central one is 5 Å. The distance from the top and bottom one to the central is 4.5 Å. The superimposed grid reveals furthermore a very interesting phenomenon: At the position between the CO molecules is a bare copper atom with no adsorbent sitting on top of it. There the depression is actually the deepest. This position will be referred as to the empty lattice site. The line scan in figure 5.8 over the vertical CO molecules demonstrates this

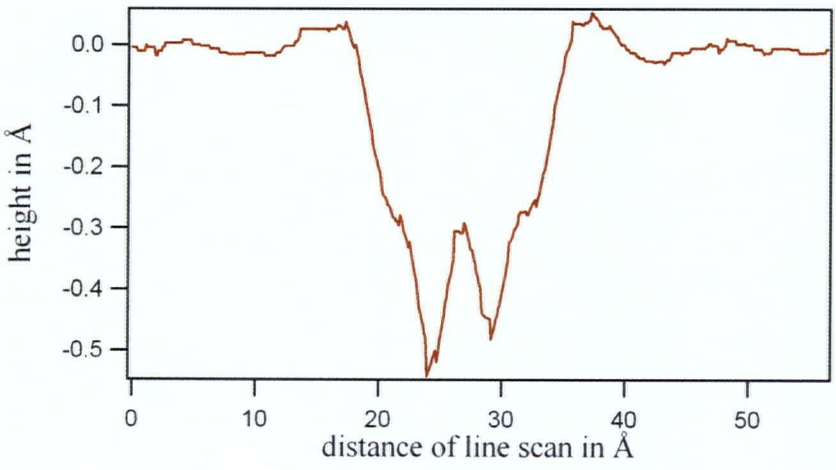

Figure 5.8: Line scan over the vertical line of the CO molecules in figure 5.7. The deepest depressions are at the two bare Cu (111) lattice sites without an adsorbate.

phenomenon more depictive.

This is first counterintuitive since there is no adsorbate contributing with a destructive tunneling channel. This phenomenon, however, can be partly explained by taking the Gaussian shaped depression with a width of 10 Å into account. Superimposing these Gaussian depressions with a small shift of their maxima will show a maximum depression at the empty lattice sites. In terms of the Green's function approach there is twice the influence of the destructive tunneling channels T_2 and T_3 at the empty lattice site. Obviously it is not the full amplitude of T_2 since its influence decays exponentially with the distance from the adsorption site.

To simulate this superposition, an inverted line scan over a single CO molecule was used to simplify the calculation, shown in figure 5.9. Three of these line scans were summed with their maxima shifted relative to each other to simulate three adjacent CO molecules. The single line scan for

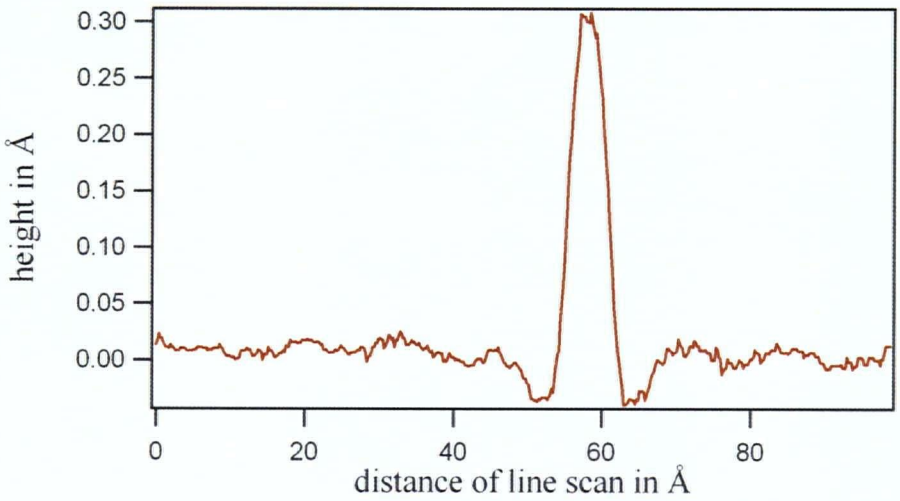

Figure 5.9: Inverted line scan over a single CO molecule from image in Fig. 5.6.

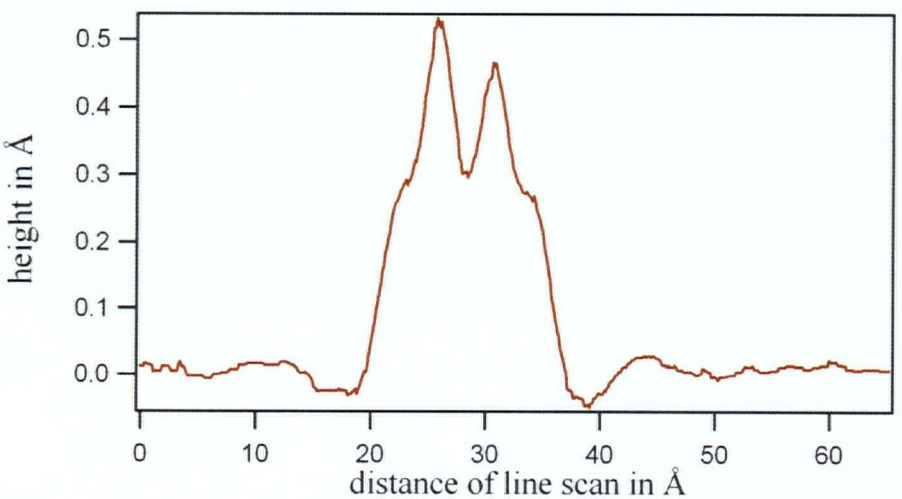

Figure 5.10: Inverted line scan along the vertical aligned CO molecules in figure 5.7. This line scan is the average of 10 vertical line scans.

the simulation and the line scans over the plus sign were taken from the same image for a sound comparison. The image used (figure 5.11) shows the cluster and additional isolated CO molecules. This image was then flattened and inverted. After that the line scans across the plus sign and an isolated CO molecule were taken, shown in figure 5.9 and figure 5.10. Using the same data guarantees the same imaging properties, like tip, bias and current. The additional image formatting before taking the line scans ensures that simulation and actual line scan are based on the same conditions. This is important to get a conclusive comparison between the simulated line scan and the actual line scan over the plus sign.

The first simulated line scan (figure 5.12 a)) was done by adding three single line scans with a distance between the maxima of 4.5 Å to simulate three CO molecules aligned, 4.5 Å apart on an underlying copper substrate, which is imaged as a flat terrace with an average height of 0 Å.

Comparing now the simulated line scan over three molecules in figure 5.12 a) to the actual inverted line scan in figure 5.12 b) over the vertical line of molecules, one can see immediately an agreement of the shape. The actual line scan shows two peaks where one is higher then the other. This difference in the form could be only reproduced in the simulated line scan by placing one of the CO molecules not exactly on top of a Cu lattice site, but 0.05 Å away from the center. The two peaks are at the position of the empty lattice sites between the adsorption sites. The higher protrusion in the actual line scan is 0.54 Å whereas in the simulated case it is 0.34 Å. The discrepancy is with 0.2 Å substantial, considering the noise of 0.01 Å. This means that the simple model of superimposing the different interfering tunneling channels does not

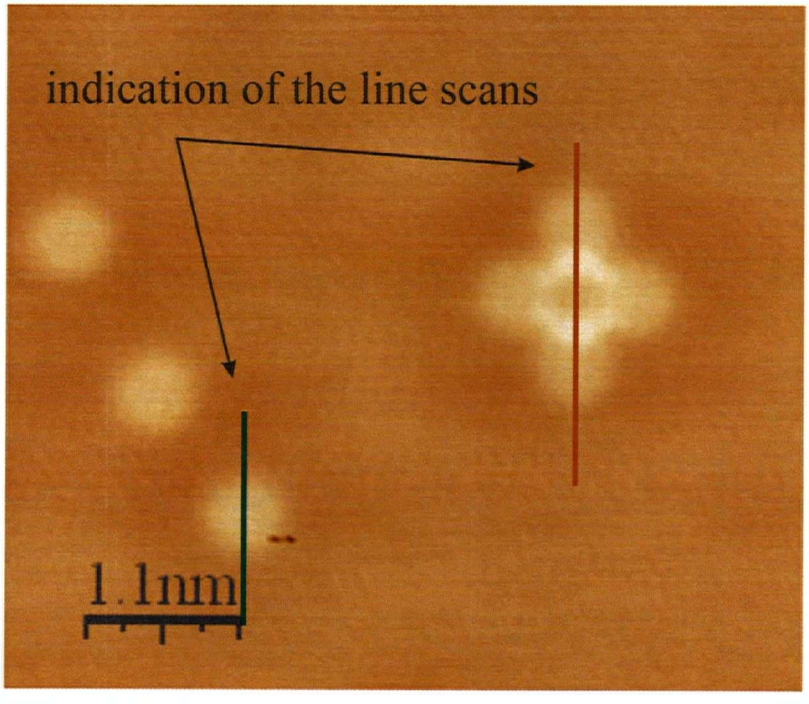

Figure 5.11: Image of the CO cluster forming a plus sign with additional isolated CO molecules. Taken with a bias of 0.3 V and tunneling current of 8 nA at 18 K. The red lines indicate the line scans.

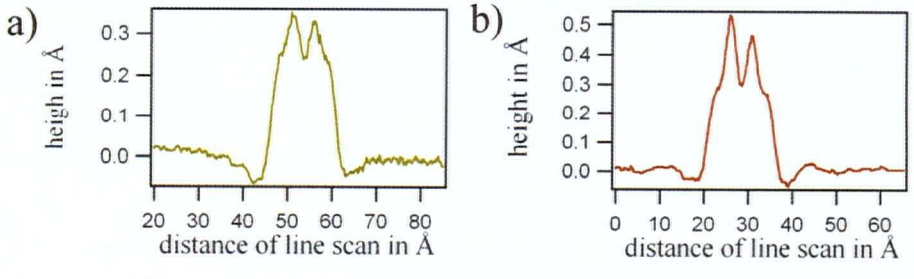

Figure 5.12: a) Simulation of a molecular row of 3 CO's by a sum of three single line scans, shifted relative to each other by 4.5 Å. The location of the two peaks are the copper lattice sites with no adsorbate between the adsorption sites. b) Observed inverted line scan from figure 5.10.

yet explain the full effect. The discrepancy of the contrast is smaller at the CO adsorption sites, but relatively there are both approximately 60%. The location of the adsorption site appear in the actual line scan as a protrusion of 0.3 Å whereas in the simulated version as a protrusion of 0.2 Å. The width in both cases agrees very well to be 18 Å.

The next step for a simulation is to include the influence of the two CO molecules sitting to the left and to the right of the central CO molecule. Therefore a Cu lattice grid was superimposed on an isolated CO molecule. A line scan was taken 5.1 Å next to the single CO molecule, over the Cu lattice site where the vertical CO molecules would be aligned, illustrated in figure 5.13. This inverted line scan appears as a small depression at the position of the vertical line. This depression can be explained by standing surface waves, as illustrated earlier.

If now this additional line scan is added twice to the previous simulated line scan including the contribution from all 5 isolated molecules the peak amplitude actually decreased to 0.27 Å. This is shown in figure 5.14. Now the discrepancy between the highest peaks of actual line scan and simulated line scan increased to 0.27 Å. This means that by using the simple model, the Green's function approach would suggest, it is not possible to explain this effect.

The same analysis can be done for the horizontal line scan. Figure 5.15 a) shows the actual horizontal line scan over the inverted plus sign. The effect of two higher peaks at the empty lattice sites is also visible, however with 0.36 Å not as distinct as in the vertical case. This can be explained by the larger distance of 5.1 Å between the horizontal sitting CO molecules

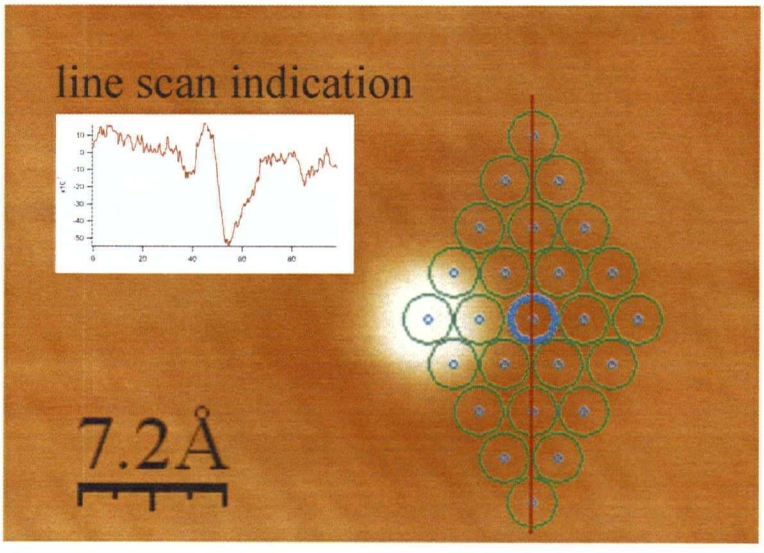

Figure 5.13: The red line shows the line scan taken at the position where in the plus sign the vertical sitting CO molecules would sit. The influence of the isolated CO molecule at that position is then added to the simulated vertical line scan.

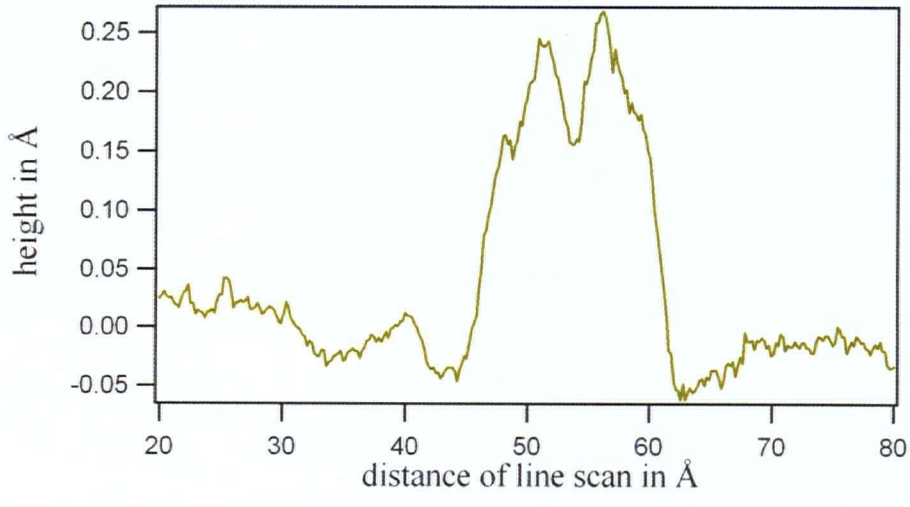

Figure 5.14: Sum of three single line scans, shifted to each other with 4.5Å, plus two lines cans as shown in figure 5.13 to simulate the influence of all 5 CO molecules.

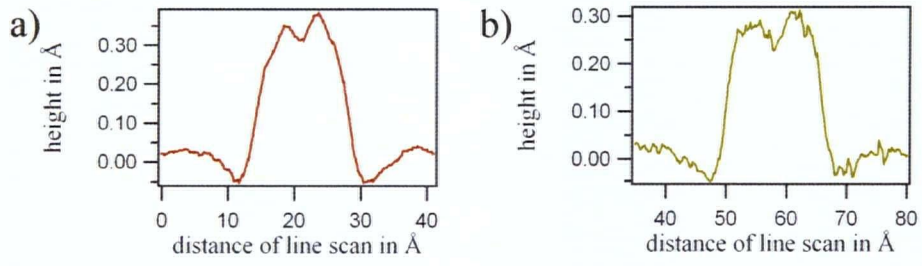

Figure 5.15: a) Shows the actual horizontal line scan over 3 CO molecules in the plus sign. b) The sum of three line scans, shifted relative to each other by 5.1Å.

compared to 4.5 Å between the vertical ones.

The horizontal line scan can again be simulated with the sum of 3 single line scans sitting now 5.1 Å apart as shown in figure 5.15 b). It shows a similar shape to the actual line scan with the same width of approximately 19 Å and a difference in the maximum peak height of 0.05 Å. The simulation including all 5 CO molecules led again to a decrease in amplitude. However, the shape was very distorted and did not compare to the actual line scan. Therefore it was not considered for this analysis.

The question is now how to interpret the reported discrepancy. There are three possibilities which come to mind. One is a possible tilt of the CO molecules sitting close to each other. A second possibility would be the influence of standing waves of the surface states and third the dipole influence of the polarized CO molecules of the electronic states of copper.

Isolated CO molecules stand perpendicular to the surface on the top lattice sites. If now two CO molecules are placed next to each other on neighboring copper lattice sites they form a dimer. The ab-initio calculations by Persson [57] and Gajdot at al. [58] indicate an angle between the two

molecules of $7 - 10°$ from each other. This is due to a short range steric repulsion between the molecules [59]. Nieminen calculated that such a tilt would lead to a contribution of the tunneling current from the CO's $2\pi^*$ orbital. The tilt leads to a small protrusion between the molecules in the STM image. The molecules themselves appear still as a depression. This effect was also observed by S. Zöephel et al [42] and Heinrich et al [60]. But that means for our case that the CO molecules in the plus sign are not tilted. First the short range steric repulsion forces drop exponentially and are essentially zero at a distance of 4 Å [59]. Second, in case of a tilt we should have seen a protrusion between the molecules and not a deeper depression. Therefore this interpretation fails.

The second possibility would be that standing waves of the Cu (111) surface, which modulate the appearance of the plus sign. But as discussed for the addition of a fourth and fifth molecule to the simulation, the influence of the surface states would have the opposite effect than the one we try to explain. Furthermore the amplitudes of these surface states are around 0.03 Å which would not add up to a difference of over 0.2 Å.

The case of the dipole field due to the polarized molecule is an interesting approach, although difficult to calculate. The CO molecule has due to the different electronegativity of C and O a dipole moment. This results into an electric field and therefore to a local work function change at the adsorption site. It is not unreasonable to expect an influence of this field to the occupation of the electronic states of the local copper atoms. This influence would be difficult to observe on an isolated adsorbed CO molecule, since this effect would mangle with the destructive interference of the different tunnel-

ing channels. In the case of the described plus sign, one can imagine that in the region of the cluster electronic states are depleted of electrons. This would lead to a decrease of the LDOS above the copper atom between the decorated lattice sites and could therewith be an explanation for a lower depression then expected. The given arguments are not conclusive, however, reports in the literature can be found describing such a phenomenon: The first one was Sautet [26] who described the possibility of such an influence due to the tip bias itself, though, he concluded that this influence would be negligible. Yet, Limot [61] showed experimentally a shift in the surface-stark effect on Ag(111) related to the applied bias voltage. This leads in fact to an influence on the electronic states of Ag(111) due to the field induced by the tip.

Such an effect would raise the question how strong this influence is and how it affects the density of states. This would become especially important for the imaging characteristics of larger molecules. A comparison of the experimental image to a theoretical calculation of the respective data without the influence of an additional electric field might lead to misinterpretation of the molecule's contrast.

With this experiment it was possible to test the Green's function approach on single CO molecules as well as clusters of CO molecules. The theory explains the contrast of single CO molecules but can not explain fully the contrast observed in case of a cluster of CO molecules. The effect in case of CO is not large. However, if the reason for the increased depression is the dipole moment of the CO molecule the effect of an electric field on the contrast of larger adsorbates has to be investigated.

5.2 CO manipulation

The precise manipulation of atoms and molecules is one of the most fascinating and important procedure in nanoscale science. It allows to structure matter at the atomic scale.

To test the manipulation abilities of our LT-STM the system CO on Cu was used [33, 50, 51, 52, 53]. The parameters of the manipulation are well known and it is possible to do illustrative manipulation as will be shown below. Furthermore it was possible, as demonstrated in the imaging section, to build patterns to test the most recent imaging theories.

In the following I will give a brief introduction in manipulation techniques, demonstrate the manipulation of single CO molecules to nanoscale ensembles and the optimization of the manipulation parameters.

There are two major manipulation techniques, vertical and lateral manipulation. In the case of vertical manipulation, the adsorbate is transferred to the tip by a bias voltage pulse and is then positioned by a second pulse. The lateral manipulation, which is used in this work, uses the tip to push or pull the adsorbate to the desired position.

In the lateral manipulation the CO is pushed by the tip over the lattice as schematically shown in figure 5.16. The tip is positioned behind the CO molecule and approached close to the surface by applying small voltages (0.05 V) and high currents(80 nA). Then the tip is moved towards the CO which feels increasing repulsive forces due to wave function overlap with the tip and jumps to the next lattice site.

The jumping from one lattice site to the next can be observed in the tip height and therewith the tunneling current. Figure 5.17 shows the sawtooth

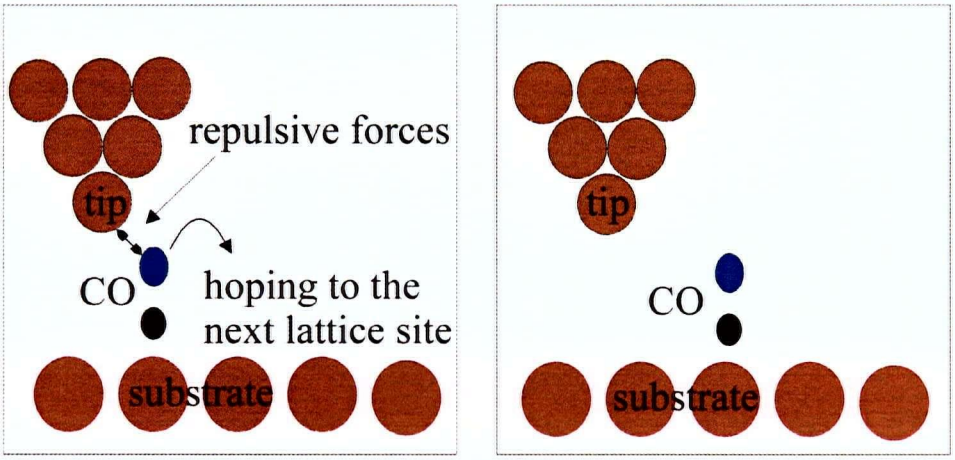

Figure 5.16: schematic drawing of the CO manipulation. The tip is positioned next to the CO molecule and close over the substrate. By moving the tip towards the CO, repulsive forces between tip and molecule increase and the CO jumps to the next lattice site.

form of the vertical tip position while a CO molecule was pushed over 26 lattice sites along a close packed copper row. Whenever the tip approached the CO molecule and the repulsion force increased the current decreased. This is simply due to the discussed depressing imaging properties of CO on Cu(111). Once the repulsive force gets large enough the CO molecule hops to the next lattice site which appears as a sudden increase in the current. Each sawtooth segment represents with approximately 2.5 Å a jump from one substrate lattice site to the next.

Figure 5.18 shows the image before and after manipulation of two CO molecules, indicated with red arrows. The first image shows two CO molecules and the path selected for the tip to move as well as their target position, indicated by the red dotted circles. In the second image both manipulation steps are indicated. The two CO's were successfully moved from their for-

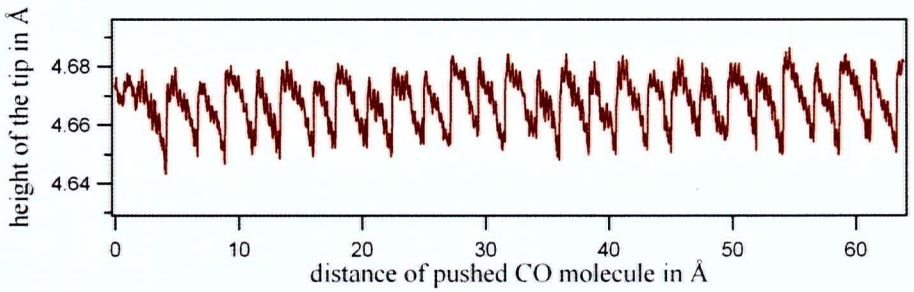

Figure 5.17: This shows the sawtooth behavior of the tip height and current in a linear manipulation of a CO molecule over a distance of 60 Å.

mer position indicated with a blue dotted circle to the desired position. The sawtooth like tip movement over the pushed distance is shown for both manipulation steps. One reason for the difference in form is that the COs were pushed along different directions on the substrate lattice.

In this case every step of the manipulation was successful, however, in general with the above described parameters the efficiency was much lower and depended strongly on the tip condition. Manipulating along the closed packed copper rows increased the success rate. Using these principles "UBC" was written with 28 CO molecules, shown in Figure 5.19. The operation took 30 consecutive hours.

The next test for the stability of the STM was how many days would the tip stay over the same place, doing manipulation. Therefore "CFI" was written (see figure 5.21), which took again over 30 hours but stretched over 4 days. The movie of the single manipulation steps can be seen at `http://www.physics.ubc.ca/~stm`. The biggest concern was the refilling of the cryostat, for which the chamber had to be directly connected to the transfer line and therewith vibrations are transmitted to the STM. This prob-

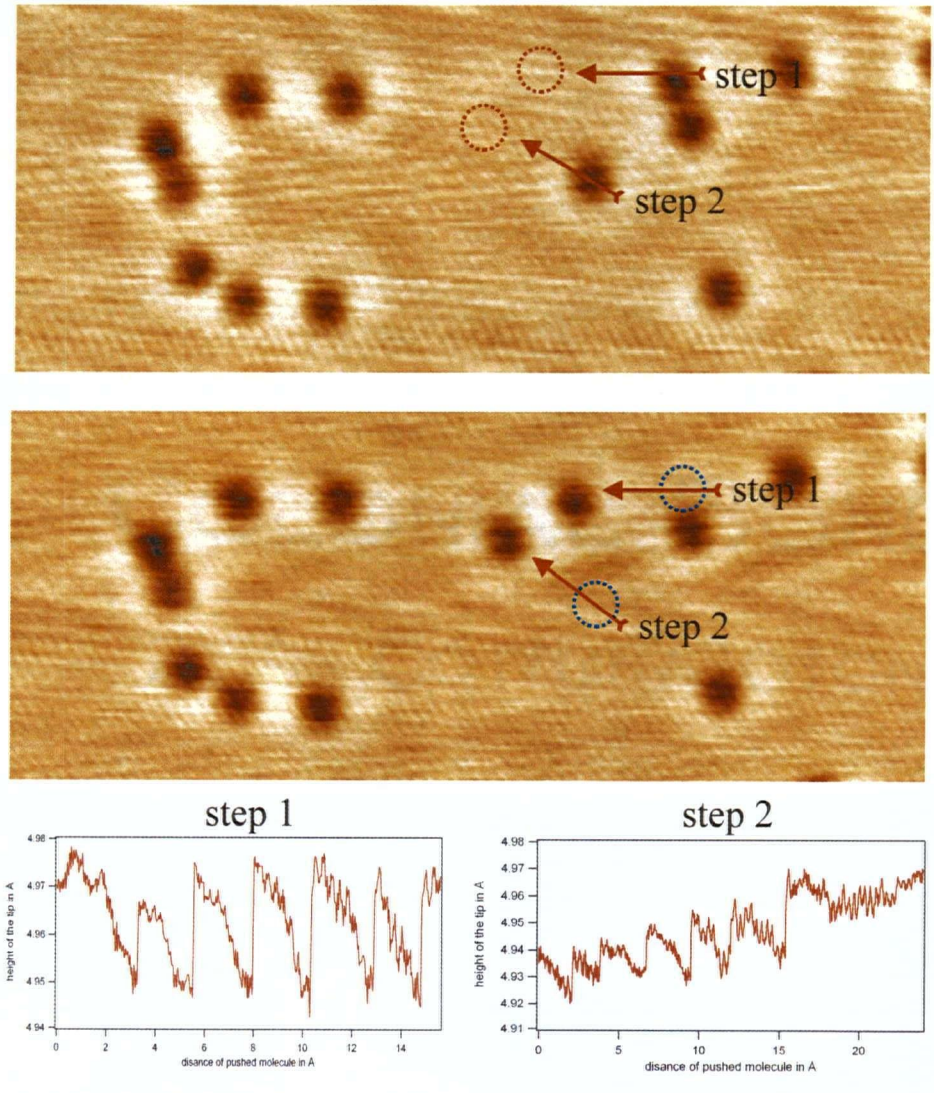

Figure 5.18: Manipulation of two CO molecules. The first image shows the two CO molecules, which will be displaced. The direction and length the tip will push them is indicated with the two arrows and the desired new position is indicated with a red dotted circle. The second image shows the successful manipulation from the original position, indicated by the blue dotted circle. The last two images show the sawtooth like tip movement during the manipulation.

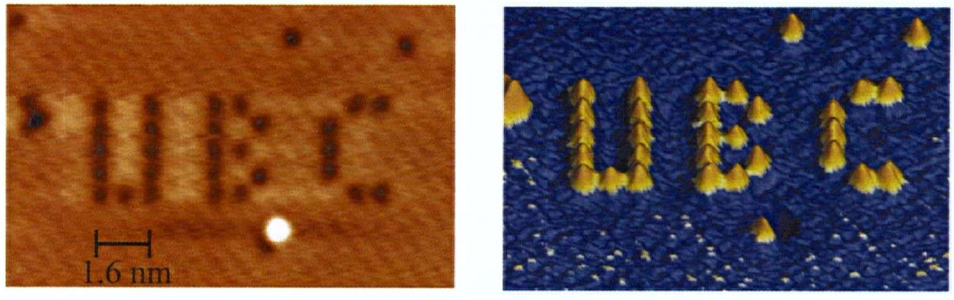

Figure 5.19: Our first nano structure using CO molecules to "write" UBC on Cu(111). The first image are the raw data after the manipulation. The second image shows an inverted, three dimensional view on the UBC. The substrate temperature was 18 K, the applied bias was 0.065 V and the tunneling current 0.52 nA.

lem was solved with an elaborated filling procedure and the manipulation over four days was successful. Figure 5.21 shows extracts of the manipulation steps, which were put together to a movie to show the local stability of the manipulation over four days. The stability of the tip over four days was a success as well, especially during manipulation experiments, since it is the most delicate and crucial element in STM work.

The last manipulation experiment and test was to find optimized manipulation parameters for CO on Cu(111). The parameters include the tip condition, applied bias and tunneling current during the manipulation. In general, it was found that the better the imaging contrast is, the higher the success rate of manipulation. Good contrast is an indication of a sharp and stable tip which seemed to be also beneficial for manipulation purposes which makes sense since the tip atom and therewith its orbital stick far out of the apex. The for this work and in the literature used manipulation current of 80 nA was the maximum possible, before crashing the tip into the sample.

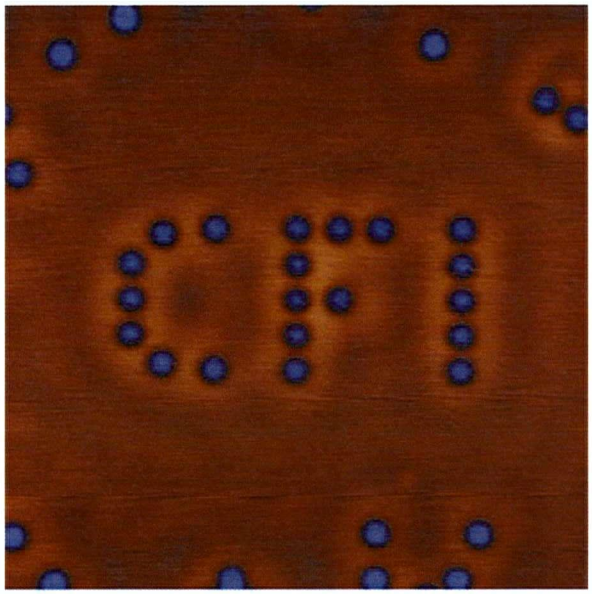

Figure 5.20: The CFI image after 4 days of manipulation. It furthermore shows that science can become art

The applied bias was varied and in case of changing the bias and its polarization from 0.05 V to -0.07 V the success rate was increased drastically. This was used to the manipulation shown in figure 5.22. With 22 CO molecules "A+K" was written in 4 hours with the optimized parameters. This image includes furthermore the plus sign which was analyzed in section 5.1. A complete conclusion how to interpret the character of the repulsive forces between tip and CO molecule could not yet be established.

We showed that it is possible with our LT-STM to manipulate CO molecules to atomically precise ensembles. Furthermore its stability over several days was demonstrated. The manipulation tests with the new LT STM were very successful and are an important knowledge for our further studies. Finally we were able to optimize the efficiency in manipulating CO molecules

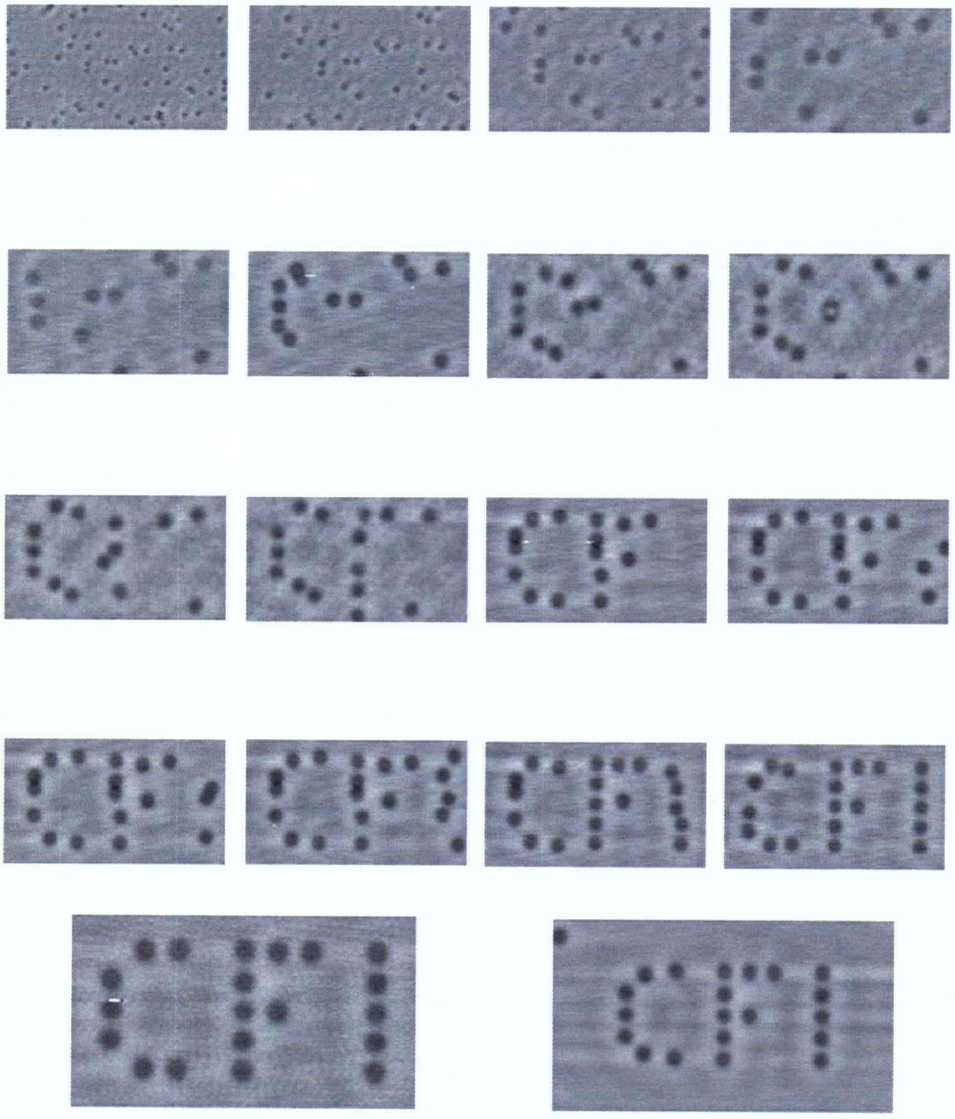

Figure 5.21: Development phases in writing "CFI" with CO molecules on Cu(111). Most of the images are 90 by 48 Å. The first four are a zoom from 250 by 135 Å to 90 by 60 Å. The last image is 110 by 60 Å. The substrate temperature was 18 K , the applied bias 0.3 V and the tunneling current 0.8 nA. The movie can be watched at `http://www.physics.ubc.ca/~stm`

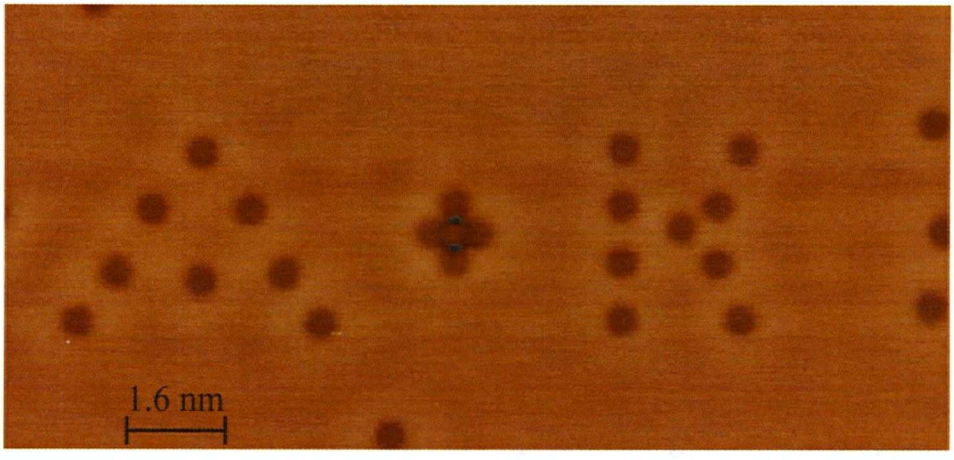

Figure 5.22: The anagram "A+K" was assembled in 4 hours out of 22 CO molecules on Cu(111). The substrate temperature was 18 K , the applied bias 0.3 V and the tunneling current 0.8 nA.

on Cu(111).

Chapter 6

Conclusion

In this work a Low-Temperature Scanning Tunneling Microscope was assembled, tested, calibrated and first molecular manipulation and atomic imaging experiments were carried out.

The LT-STM can be cooled with a bath cryostat to 5 K and reaches currently an equilibrium temperature of 10 K. The STM temperature can be continuously varied between 10 K and room temperature. The preparation of samples takes place in a separate chamber, whereby the sample temperature can be varied between 50 K and 800 K. This allows a very large spectrum of preparation possibilities for the study of self-assembled nanostructures. To test the quality of the substrate surface as well as a first surface analysis after the preparation a LEED was mounted on the preparation chamber.

The STM is enclosed in radiation shields cooled by the bath cryostat, which acts like a cryo pump. Therefore the sample stays uncontaminated over several weeks in the STM. The cooled down STM had a vertical resolution of 0.01 Å and stays stable over the same sample region for several days. This allows atomic resolution and tunneling spectroscopy studies. Therewith atomic resolution images of closed packed metal surfaces and standing wave patterns were obtained.

On Cu (111) a small amount of CO was adsorbed and analyzed. For the interpretation of the CO imaging characteristics the most recent imaging the-

ories were used and it could be shown that an increased depression over bare Cu lattice sites between CO molecules could still not be entirely explained. One possibility causing this effect might be the depletion of occupied states in the region of the CO cluster caused by the polarized CO molecule.

We achieved atomically precise manipulation of single CO molecules and a series of nanoscale structures were fabricated. Writing with molecules was a first time achievement in Canada.

6.1 Outlook

With the completed assembly of the LT-STM and its successful testing we can begin now our study on molecular self-assembly and engineering. Currently the research addresses metal-directed assembly of functional porphyrine molecules. This research is the systematic and synergetic interdisciplinary study of functional molecules and supramolecular architectures at the nanoscale. These efforts contribute to the development of novel bottom-up fabrication techniques and functional materials to be employed in future nanoscale devices and systems constructed from both inorganic and organic components.

The aspect of a possible influence of polarization on the STM imaging is an important topic for imaging larger molecules. For the interpretation of larger adsorbate's absorption sites on a substrate as well as to interpret their contrast often theoretical calculations have to be consulted. If the polarization of the molecule and furthermore the field of the tip has an influence on the adsorbate's contrast it is crucial to investigate to which degree this effect influences the imaging properties, to avoid misinterpretations of STM

images.

Bibliography

[1] G. Binnig, H. Rohrer, Ch. Gerber, and E. Weibel, "Surface studies by Scanning Tunneling Microscopy", *Physical Review Letters*, vol. 49, pp. 57, 1982.

[2] G. Binnig, H. Rohrer, Ch. Gerber, and E. Weibel, "Tunneling through a controllable vacuum gap", *Applied Physics Letters*, vol. 40, pp. 178, 1982.

[3] G. Binnig, H. Rohrer, Ch. Gerber, and E. Weibel, "7 x 7 reconstruction on Si(111) resolved in real space", *Physical Review Letters*, vol. 50, pp. 120, 1983.

[4] D.M. Eigler and E.K. Schweizer, "Positioning single atoms with Scanning Tunnelling Microscope", *Nature*, vol. 344, pp. 6266, 1990.

[5] Stroscio, A. Joseph, and D.M. Eigler, "Atomic and molecular manipulation with the Scanning Tunneling Microscope", *Science*, vol. 254, pp. 1319, 1991.

[6] L.J. Whitman, Stroscio, A. Joseph, R.A. Dragoset, and R.J. Celotta, "Manipulation of adsorbed atoms and creation of new structures on room-temperature surfaces with a Scanning Tunneling Microscope", *Science*, vol. 251, pp. 1206, 1991.

[7] S.W. Hla, L. Bartels, G. Meyer, and K.H. Rieder, "Inducing all steps of a chemical reaction with the Scanning Tunneling Microscope tip: Towards single molecule engineering", *Physical Review Letters*, vol. 85, pp. 2777, 2000.

[8] L.J. Lauhon and W. Ho, "Control and characterization of a multistep unimolecular reaction", *Physical Review Letters*, vol. 84, pp. 1527, 2000.

[9] B.C. Stipe, M.A. Rezaei, W. Ho S. Gao, M. Persson, and B.I. Lundqvist, "Single-molecule dissociation by tunneling electrons", *Physical Review Letters*, vol. 78, pp. 4410, 1997.

[10] J.V. Barth, T. Zambelli, J. Wintterlin, R. Schuster, and G. Ertl, "Direct observation of mobility and interactions of oxygen molecules chemisorbed on the Ag(110) surface", *Physical Review B*, vol. 55, pp. 12902, 1997.

[11] J. Repp, G. Meyer, F.E. Olsson, and M. Persson, "Controlling the charge state of individual gold adatoms", *Science*, vol. 305, pp. 493, 2004.

[12] F. Rosei, M. Schunack, Y. Naitoh, P. Jiang, A. Gourdon, E. Læsgaard, C. Joachim I. Stensgaard, and F. Besenbacher, "Properties of large organic molecules on metal surfaces", *Progress in Surface Science*, vol. 71, pp. 94, 2003.

[13] S. Stepanow, M. Lingenfelder, A. Dmitriev, H. Spillmann, E. Delvigne, N. Lin, X. Deng, C. Cai, J.V. Barth, and K. Kern, "Steering molecular organization and hostguest interactions using two-dimensional

nanoporous coordination systems", *Nature Materials*, vol. 3, pp. 229, 2004.

[14] J.V. Barth, H. Brune, B. Fischer, J. Weckesser, and K. Kern, "Dynamics of surface migration in the weak corrugation regime", *Physical Review Letters*, vol. 84, pp. 1732, 2000.

[15] H.A. Mizes, S. Park, and W. A. Harrison, "Multiple-tip interpretation of anomalous Scanning Tunneling Microscopy images of layered materials", *Physical Review B*, vol. 36, pp. 4491, 1987.

[16] W.A. Hofer, A.S. Foster, and A.L. Shluger, "Theories of Scanning Probe Microscopes at the atomic scale", *Review of Modern Physics*, vol. 75, pp. 1287, 2003.

[17] M. Yu, M.J. Dyer, G.D. Skidmore, H.W. Rohrs, X. Lu, K.D. Ausman, J.R. von Ehr, and R.S. Ruoff, "Three-dimensional manipulation of carbon nanotubes under a scanning electron microscope", *Nanotechnology*, vol. 10, pp. 244, 1999.

[18] D. Drakova, "Theoretical modeling of Scanning Tunneling Microscopy, Scanning Tunneling Spectroscopy and Atomic Force Microscopy", *Reports on Progress in Physics*, vol. 64, pp. 205, 2001.

[19] J. Tersoff and D.R. Hamann, "Theory and application for the Scanning Tunneling Microscope", *Physical Review Letters*, vol. 50, pp. 1998, 1983.

[20] J. Bardeen, "Tunnelling from a many-particle point of view", *Physical Review Letters*, vol. 6, pp. 57, 1961.

[21] W.A. Hofer, "Challenges and errors: interpreting high resolution images in Scanning Tunneling Microscopy", *Progress in Surface Science*, vol. 71, pp. 147, 2003.

[22] C.J. Chen, "Effect of m 0 tip states in Scanning Tunneling Microscopy: the explanation of corrugation reversal", *Physical Review Letters*, vol. 69, pp. 1656, 1992.

[23] R. Wisendanger and H.J.Guentherodt, *Scanning Tunneling Microscopy III*, Springer Series in Surface Science, 1993.

[24] N.D. Lang, "Vacuum tunneling current from an adsorbed atom", *Physical Review Letters*, vol. 55, pp. 230, 1985.

[25] N.D. Lang, "Theory of single-atom imaging in the Scanning Tunneling Microscope", *Physical Review Letters*, vol. 56, pp. 1164, 1986.

[26] P. Sautet, "Images of adsorbates with the Scanning Tunneling Microscope: Theoretical approaches to the contrast mechanism", *Chemical Review*, vol. 97, pp. 1097, 1997.

[27] J. Nieminen, S. Lahti, S. Paavilainen, and K. Morgenstern, "Contrast changes in STM images and relations between different tunneling models", *Physical Review B*, vol. 66, pp. 165421, 2002.

[28] J. Nieminen, E. Niemi, and K.H. Rieder, "Interference between competing tunneling channels anch chemical resolution of STM", *Surface Science*, vol. 552, pp. 47, 2004.

[29] CJ. Chen, *Introduction to Scanning Tunneling Micoscopy* , Oxford University Press, 1993.

[30] C.J. Chen, R. Wiesendanger, and H.J. Guentherodt, *Scanning Tunneling Micoscopy III*, Springer-Verlag, 1993.

[31] M.Tsukada, K.Kobayashi, N.Isshiki, S.Watanabe, H.Kageshima, T.Shimizu, H.J. Guntherodt, and R.Wiesendanger, *The Role of Tip Atomic and Electronic Structure on Scanning Tunneling Microscopy and Spectroscopy in "Scanning Tunneling Microcopy III"*, Springer-Verlag, 1993.

[32] R.J. Behm and W. Hoesler, *Chemistry and Physics of Solid Surfaces*, Springer-Verlag, Berlin Heidelberg New York, 1986.

[33] L. Bartels, G. Meyer, and K.H. Rieder, "Controlled vertical manipulation of single co molecules with the Scanning Tunneling Microscope: A route to chemical contrast", *Applied Physics Letters*, vol. 71, pp. 213, 1997.

[34] D.M. Eigler, P.S. Weiss, E.K. Schweizer, and N.D. Lang, "Imaging xe with a Low-Temperature Scanning Tunneling Microscope", *Physical Review Letters*, vol. 66, pp. 1189, 1991.

[35] W. Hebenstreit, J. Redinger, Z. Horozova, M. Schmid, R. Podloucky, and P. Varga, "Atomic resolution by STM on ultra-thin films of alkali halides: experiment and local density calculations", *Surface Science*, vol. 424, pp. 321, 1999.

[36] K. Glöckler, M. Sokolowski, A. Soukopp, and E. Umbach, "initial growth of insulating overlayers of NaCl on Ge(100) observed by Scanning Tunneling Microscopy with atomic resolution", *Physical Review B*, vol. 54, pp. 7705, 1996.

[37] E. Kopatzki and R.J. Behm, "STM imaging and local order of oxygen adlayers on Ni(100)", *Surface Science*, vol. 245, pp. 255, 1991.

[38] W. Kohn and L.J. Sham, "Self-consistent equations including exchange and correlation effects", *Physical Review A*, vol. 140, pp. 1133, 1965.

[39] G. Doyen, E. Koetter, J.P. Vigneron, and M. Scheffler, "Theory of Scanning Tunneling Microscopy", *Applied Physics A*, vol. 51, pp. 281, 1990.

[40] P. Sautet and C. Joachim, "Electronic transmission coefficient for the single-impurity problem in the scattering-matrix approach", *Physical Review B*, vol. 38, pp. 12238, 1988.

[41] P. Sautet and M.L. Bocquet, "STM and chemistry: A qualitative molecular orbital understanding of the image of CO on a Pt surface", *Surface Science*, vol. 360, pp. 28, 1996.

[42] S. Zöphel, J. Repp, G. Meyer, and K.H. Rieder, "Determination of binding sites in ordered phases of CO/Cu(211) employing molecular level manipulation", *Chemical Physics Letters*, vol. 310, pp. 137, 1999.

[43] A.J. Heinrich, C.P. Lutz, J.A. Gupta, and D.M. Eigler, "Molecule Cascades", *Science*, vol. 298, pp. 1381, 2002.

[44] E. Niemi and J. Nieminen, "Molecular reorientation in assembeled CO structures and contrast inversion in STM", *Chemical Physics Letters*, vol. 397, pp. 200, 2004.

[45] P. Sautet, "Atomic adsorbate identification with the STM: a theoretical approach", *Surface Science*, vol. 374, pp. 406, 1997.

[46] J.B. Pendry, A.B. Pretre, and B.C.H. Krutzen, "Theory of the Scanning Tunnelling Microscope", *Journal of Physics: Condensed Matter*, vol. 3, pp. 4313, 1991.

[47] T.N. Todorov, G.A.D. Briggs, and A.P Sutton, "Elastic quantum transport through small structures", *Journal of Physics: Condensed Matter*, vol. 5, pp. 2389, 1993.

[48] J.P. Ibe, P.P. Bey, S.L. Brandow, R.A. Brizzolara, N.A. Burnham, D.P. DiLella, K.P. Lee, C.R.K. Marrian, and R.J. Colton, "On the electrochemical etching of tips for Scanning Tunneling Microscopy", *Journal of Vacuum Science and Technology A*, vol. 8, pp. 3570, 1990.

[49] L. Petersen, P. Laitenberger, E. Lægsgaard, and F. Besenbacher, "Screening waves from steps and defects on Cu (111) and Au (111) imaged with STM: Contribution from bulk electrons", *Physical Review B*, vol. 58, pp. 7361, 1998.

[50] G. Meyer and K.H. Rieder, "Controlled manipulation of single atoms and small molecules with the Scanning Tunneling Microscope", *Surface Science*, vol. 1087, pp. 377, 1997.

[51] B. Neu, G. Meyer, and K.H. Rieder, "Controlled vertical and lateral manipulation of single atoms and small molecules with the Scanning Tunneling Microscope ", *Modern Physics letters B*, vol. 9, pp. 963, 1995.

[52] L. Bartels, G. Meyer, and K.H. Rieder, "Basic steps involved in the lateral manipulation of single CO molecules and roes of CO molecules", *Chemical Physics Letters*, vol. 273, pp. 371, 1997.

[53] L. Bartels, G. Meyer, and K.H. Rieder, "Basic steps of lateral manipulation of single CO molecules and diatomic clusters with a Scanning Tunneling Microsope tip", *Physical Review Letters*, vol. 79, pp. 697, 1997.

[54] L. Bartelsand G. Meyer and K.H. Rieder, "The evolution of CO adsorption on Cu(111) as studied with bare and CO-functionalized scanning tunneling tips", *Surface Science*, vol. 432, pp. 621, 1999.

[55] J. Camarero, L. Spendeler, G. Schmidt, K.H. Heinz, J.J. de Miguel, and R. Miranda, "Surfactant-induced suppression of twin formation during growth of fcc Co/Cu superlattices on Cu(111)", *Physical Review Letters*, vol. 73, pp. 2448, 1994.

[56] M. Gajdos, A. Eichler, and J. Hafner, "Co adsorption on close-packed transition and noble metal surfaces: trends from ab initio calculations", *Journal of Physics: Condensed Matter*, vol. 16, pp. 1141, 2004.

[57] M. Persson, "Theory of elastic and inelastic tunnelling microscopy and spectroscopy: CO on Cu revisited: One contribution of 12 to a discussion

meeting 'organizing atoms: manipulation of matter on the sub-10 nm scale"', *Philosophical Transactions of the Royal Sosciety A*, vol. 362, 2004.

[58] M. Gajdos, A. Eichler, J. Hafner, G. Meyer, and K.H. Rieder, "CO adsorption on Cu (211) surface: first principle and STM study", *arXiv:cond-mat*, vol. 2, 2004.

[59] H. Kato, M. Kawai, and J. Yoshinobu, "Switching in the molecular orientation ruled by steric repulsion of adsorbed CO on Pd (110)", *Physical Review Letters*, vol. 82, pp. 1899, 1999.

[60] A.J. Heinrich, C.P. Lutz, J.A. Gupta, and D.M. Eigler, "Molecule Cascades", *Science*, vol. 298, pp. 1381, 2002.

[61] L. Limot, T. Maroutian, P. Johansson, and R. Berndt, "Surface-state strak shift in a Scanning Tunneling Microscope", *Physical Review Letters*, vol. 91, pp. 196801, 2003.